The Pan-STARRS1 $z > 5.6$ Quasar Survey. II. Discovery of 55 Quasars at $5.6 < z < 6.5$

Eduardo Bañados[1,2] , Jan-Torge Schindler[1,3] , Bram P. Venemans[3] , Thomas Connor[2,4,5] , Roberto Decarli[6] ,
Emanuele Paolo Farina[7] , Chiara Mazzucchelli[8] , Romain A. Meyer[1] , Daniel Stern[4] , Fabian Walter[1] , Xiaohui Fan[9] ,
Joseph F. Hennawi[3,10] , Yana Khusanova[1] , Nidia Morrell[11] , Riccardo Nanni[3] , Gaël Noirot[4,12] , Antonio Pensabene[13] ,
Hans-Walter Rix[1] , Joseph Simon[4,14] , Gijs A. Verdoes Kleijn[15] , Zhang-Liang Xie (谢彰亮)[1] ,
Da-Ming Yang (羊达明)[3] , and Andrew Connor[16]

[1] Max Planck Institut für Astronomie, Königstuhl 17, D-69117, Heidelberg, Germany; banados@mpia.de
[2] The Observatories of the Carnegie Institution for Science, 813 Santa Barbara Street, Pasadena, CA 91101, USA
[3] Leiden Observatory, Leiden University, Niels Bohrweg 2, 2333 CA Leiden, The Netherlands
[4] Jet Propulsion Laboratory, California Institute of Technology, 4800 Oak Grove Drive, Pasadena, CA 91109, USA
[5] Center for Astrophysics | Harvard & Smithsonian, 60 Garden Street, Cambridge, MA 02138, USA
[6] INAF—Osservatorio di Astrofisica e Scienza dello Spazio, via Gobetti 93/3, I-40129, Bologna, Italy
[7] Gemini Observatory, NSF's NOIRLab, 670 N Aóhoku Place, Hilo, HI 96720, USA
[8] Núcleo de Astronomía, Facultad de Ingeniová y Ciencias, Universidad Diego Portales, Av. Ejército 441, Santiago, 8320000, Chile
[9] Steward Observatory, University of Arizona, 933 N Cherry Avenue, Tucson, AZ 85721, USA
[10] Department of Physics, University of California, Santa Barbara, CA 93106, USA
[11] Las Campanas Observatory, Carnegie Observatories, Casilla 601, La Serena, Chile
[12] Department of Astronomy & Physics, Saint Mary's University, 923 Robie Street, Halifax, NS B3H 3C3, Canada
[13] Dipartimento di Fisica "G. Occhialini," Università degli Studi di Milano-Bicocca, Piazza della Scienza 3, I-20126, Milano, Italy
[14] Department of Astrophysical and Planetary Sciences, University of Colorado, Boulder, CO 80309, USA
[15] Kapteyn Astronomical Institute University of Groningen, The Netherlands
[16] Centre for Ancient Cultures, Monash University, Clayton, Vic 3800, Australia

Abstract

The identification of bright quasars at $z \gtrsim 6$ enables detailed studies of supermassive black holes, massive galaxies, structure formation, and the state of the intergalactic medium within the first billion years after the Big Bang. We present the spectroscopic confirmation of 55 quasars at redshifts $5.6 < z < 6.5$ and UV magnitudes $-24.5 < M_{1450} < -28.5$ identified in the optical Pan-STARRS1 and near-IR VIKING surveys (48 and 7, respectively). Five of these quasars have independently been discovered in other studies. The quasar sample shows an extensive range of physical properties, including 17 objects with weak emission lines, 10 broad absorption line quasars, and 5 objects with strong radio emission (radio-loud quasars). There are also a few notable sources in the sample, including a blazar candidate at $z = 6.23$, a likely gravitationally lensed quasar at $z = 6.41$, and a $z = 5.84$ quasar in the outskirts of the nearby ($D \sim 3$ Mpc) spiral galaxy M81. The blazar candidate remains undetected in NOEMA observations of the [C II] and underlying emission, implying a star formation rate <30–$70 \, M_\odot \, \mathrm{yr}^{-1}$. A significant fraction of the quasars presented here lies at the foundation of the first measurement of the $z \sim 6$ quasar luminosity function from Pan-STARRS1 (introduced in a companion paper). These quasars will enable further studies of the high-redshift quasar population with current and future facilities.

Unified Astronomy Thesaurus concepts: Quasars (1319); Active galactic nuclei (16)

Supporting material: machine-readable tables

1. Introduction

As the most luminous nontransient sources in the universe, quasars enable the study of structure formation, supermassive black holes, massive galaxies, and the intergalactic medium—at unrivaled detail—when the universe was less than a billion years old (or redshifts $z > 5.6$).

The advent of various multiwavelength large sky surveys led to a drastic increase in the number of $z > 5.6$ quasars in the past decade, at both the bright ($M_{1450} \lesssim -25$) and faint end ($M_{1450} \gtrsim -25$). Some of the main contributors are the Panoramic Survey Telescope and Rapid Response System (Pan-STARRS1; Chambers et al. 2016), the DESI Legacy Imaging Surveys (DELS; Dey et al. 2019), and the Dark Energy Survey (DES; Abbott et al. 2018, 2021) at the bright end (e.g., Bañados et al. 2016; Reed et al. 2017; Wang et al. 2019), while at the faint end, most quasars come from the Subaru High-z Exploration of Low-Luminosity Quasars survey (SHELLQs; e.g., Matsuoka et al. 2018, 2022).

This paper presents the discovery of 55 bright quasars at $5.6 < z < 6.5$. Most of them were selected from Pan-STARRS1 following the methods outlined in detail in Bañados et al. (2016). Seven of the quasars were selected from the VISTA Kilo-Degree Infrared Galaxy survey (VIKING; Edge et al. 2013), following the strategy presented by Venemans et al. (2015).

The quasars presented in Bañados et al. (2016) nearly doubled the number of $z > 5.6$ quasars known at the time, enabling a transition from studies of individual sources to statistical analyses of the quasar population in early cosmic times. For example, the much enlarged quasar sample enabled (i) the measurement of the nuclear chemical enrichment, black hole mass, and Eddington ratio distributions (e.g., Schindler et al. 2020; Farina et al. 2022; Lai et al. 2022; Wang et al. 2022), (ii) the characterization of their X-ray (e.g., Vito et al. 2019) and

radio (e.g., Liu et al. 2021) properties, (iii) the search for signatures of outflows and black hole feedback (e.g., Meyer et al. 2019; Novak et al. 2020; Bischetti et al. 2022), (iv) a census of (atomic/molecular) gas and dust in the quasar hosts (e.g., Decarli et al. 2018; Venemans et al. 2018; Li et al. 2020; Pensabene et al. 2021; Decarli et al. 2022), including the serendipitous discovery of star-forming companion galaxies (Decarli et al. 2017), (v) the search for extended Lyα nebular emission (e.g., Farina et al. 2019) and its connection to [C II] gas (Drake et al. 2022), (vi) the quantification of the properties of water reservoirs in these quasars (e.g., Pensabene et al. 2022), (vii) the identification of a population of particularly young quasars (Eilers et al. 2020), (viii) the first constraints on quasar clustering at $z \sim 6$ (Greiner et al. 2021), (ix) the study of the environments in which these quasars reside (e.g., Mazzucchelli et al. 2017a; Farina et al. 2017; Meyer et al. 2020, 2022), (x) the study of heavy elements in intervening absorption systems at $z > 5$ (e.g., Chen et al. 2017; Cooper et al. 2019), (xi) quantitative constraints on the thermal state of the intergalactic medium at $z > 5$ (e.g., Gaikwad et al. 2020), and (xii) constraints on the end phases of cosmic reionization (e.g., Bosman et al. 2022). In addition to these population studies, the large sample of quasars also enabled the identification of exciting individual sources whose properties stand out. They have been studied in much more detail in several works (e.g., Bañados et al. 2018; Momjian et al. 2018; Bañados et al. 2019; Connor et al. 2019; Decarli et al. 2019; Connor et al. 2021b; Momjian et al. 2021; Rojas-Ruiz et al. 2021; Vito et al. 2021).

This paper is structured as follows. Section 2 describes the main selection strategies and follow-up photometry used to identify Pan-STARRS1 and VIKING quasar candidates. Section 3 presents the spectroscopic observations of the quasar discoveries and discusses some individual sources. In Section 4 we discuss the five radio-loud quasars found in this work. We summarize our results in Section 5. We note that 30 quasars presented here are part of the $z \sim 6$ Pan-STARRS1 quasar luminosity function presented in a companion paper by Schindler et al. (2023). Table 1 lists the spectroscopic observations of the quasars. Table 2 reports their coordinates and general properties, and Table 3 describes their photometry.

All magnitudes reported in the paper are in the AB system, and limits correspond to 3σ. The Pan-STARRS1 magnitudes used and reported in this paper are dereddened (Schlafly & Finkbeiner 2011). We use a standard flat ΛCDM cosmology with $H_0 = 70 \text{ km s}^{-1} \text{ Mpc}^{-1}$, $\Omega_M = 0.30$.

2. Candidate Selection

The main quasar selection procedures are described in detail in Bañados et al. (2014, 2016) for candidates selected from Pan-STARRS1 and in Venemans et al. (2015) for candidates selected with VIKING. For completeness, we briefly summarize the selection criteria below.

2.1. Pan-STARRS1 Candidate Selection

Pan-STARRS1 imaged all the sky north of decl. $-30°$ in five filters, $g_{P1}r_{P1}i_{P1}z_{P1}y_{P1}$, multiple times (Chambers et al. 2016). To select high-redshift quasar candidates, Bañados et al. (2014, 2016) used the first and second internal releases of the stacked Pan-STARRS1 catalog. This time, we used the PV3 final internal version, which is very close to the final public Pan-STARRS1 release hosted by the Barbara A. Mikulski

Archive for Space Telescopes at the Space Telescope Science Institute. The most noticeable difference is the astrometric accuracy as the public version has been tied to Gaia astrometry (Gaia Collaboration et al. 2016). Here we report the PV3 catalog entries as used in our selection, but the coordinates in Table 2 correspond to the recently updated ones[17] on 2022 June 30 using Gaia Early Data Release 3 (Gaia Collaboration et al. 2021).

In our search we exclude the region near M31 ($7° <$ R.A. $< 14°$; $37° <$ decl.$< 43°$) and the most dust obscured regions in the Milky Way, requiring a reddening of $E(B-V) < 0.3$ (Schlegel et al. 1998). This allows to find quasars in less obscured regions of the Galactic plane (even at Galactic latitude $|b| < 20°$). However, the number density of sources at these low Galactic latitudes makes it harder to efficiently find quasars. In this work, we present only one new quasar with $|b| < 20°$: P119+02 at $b = 15°.48$.

We required that at least 85% of the expected point-spread function (PSF)-weighted flux in the i_{P1}, z_{P1} and y_{P1} resides in valid pixels. We excluded sources whose measurements in the z_{P1} and y_{P1} are suspicious according to the imaging processing pipeline (Magnier et al. 2020), using the same quality flags as described in Table 6 of Bañados et al. (2014). We required our candidates to be point sources using ($-0.3 < z_{P1,ext} < 0.3$) or ($-0.3 < y_{P1,ext} < 0.3$), where mag $_{P1,ext}$ is the difference between the aperture and PSF magnitudes. This removes $\sim 92\%$ of galaxies while recovering $\sim 93\%$ of stars and $\sim 97\%$ of quasars (see Section 2.1 in Bañados et al. 2016).

To select high-redshift quasar candidates, we applied the following color and signal-to-noise ratio (S/N) requirements:

$$\text{(S/N}(g_{P1}) < 3)$$
$$((\text{S/N}(i_{P1}) \geqslant 3) \text{ AND } (i_{P1} - z_{P1} > 2.0)) \text{ OR}$$
$$(i_{P1,lim} - z_{P1} > 2.0).$$

The locations of the discovered quasars in the $i_{P1} - z_{P1}$ versus $z_{P1} - y_{P1}$ plane are shown in the left panel of Figure 1. We have additional criteria that are different when the candidates have a $z_{P1} - y_{P1} < 0.5$ color (candidates expected to be at a redshift between 5.6 and 6.2) or $z_{P1} - y_{P1} \geqslant 0.5$ (candidates expected to be at redshifts between 6.2 and 6.5). For sources with $z_{P1} - y_{P1} < 0.5$,

$$\text{S/N}(z_{P1}) > 10$$
$$\text{S/N}(y_{P1}) > 5$$
$$\text{S/N}(r_{P1}) < 3 \text{ OR } (r_{P1} - z_{P1} > 2.2).$$

And for sources with $z_{P1} - y_{P1} \geqslant 0.5$,

$$\text{S/N}(z_{P1}) > 7$$
$$\text{S/N}(y_{P1}) > 7$$
$$\text{S/N}(r_{P1}) < 3.$$

We then performed our own forced photometry (using an aperture that maximizes the S/N of stars in the field) in both the stacked and single-epoch Pan-STARRS1 images to ensure the measured colors are consistent with the cataloged ones and to remove spurious or moving objects (see Sections 2.2 and 2.3 in Bañados et al. 2014). There is no human intervention in the previous steps, but we finally visually inspect the stacked and single-epoch images to remove remaining obviously poor candidates.

---

[17] See "PS1 news" in https://panstarrs.stsci.edu and Lubow et al. (2021).

Table 1
Discovery Spectroscopic Observations of the New Quasars Presented in This Work, Sorted by R.A.

Quasar	Date	Telescope/Instrument	Exposure Time	Slit Width	QLF?
PSO J000.0416−04.2739	2021 Nov 30	P200/DBSP	1200 s	1″5	T
PSO J000.0805-18.2360	2017 May 15	Magellan/LDSS3	1800 s	1″0	F
	2018 Jun 4	Magellan/LDSS3	1500 s	1″0	
	2022 Sep 17	P200/DBSP	1200s	1″5	
PSO J001.6889−28.6783	2017 Aug 05	Magellan/LDSS3	1800 s	1″0	F
PSO J002.5429+03.0632	2021 Dec 5	P200/DBSP	1300 s	1″5	T
PSO J008.6083+10.8518	2016 Nov 30	LBT/MODS	1800s	1″2	F
PSO J017.0691−11.9919	2016 Nov 26	LBT/MODS	1800s	1″2	T
PSO J030.1387−17.6238	2021 Nov 17–18	NTT/EFOSC	9000 s	1″0–1″5	F
	2022 Sep 17	P200/DBSP	1200s	1″5	
PSO J032.91882−17.0746	2017 Sep 26	Magellan/LDSS3	700 s	1″0	F
PSO J038.1914−18.5735	2017 Sep 26	Magellan/LDSS3	1800 s	1″0	T
PSO J043.1111−02.6224	2021 Nov 19	NTT/EFOSC	2580 s	1″5	F
	2022 Sep 17	P200/DBSP	1200s	1″5	
PSO J050.5605−18.6881	2017 Sep 26	Magellan/LDSS3	1800 s	1″0	F
PSO J065.9589+01.7235	2017 Mar 06	Magellan/LDSS3	900 s	1″0	F
PSO J072.5825−07.8918	2021 Nov 30	P200/DBSP	2400 s	1″5	T
PSO J076.2344−10.8878	2022 Sep 28	P200/DBSP	1020 s	1″5	T
PSO J119.0932+02.3056	2017 Mar 06	Magellan/LDSS3	600 s	1″0	F
	2018 Jan 25	Magellan/LDSS3	900 s	1″0	
PSO J124.0032+12.9989	2021 Dec 5	P200/DBSP	1200 s	1″5	T
PSO J127.0558+26.5654	2021 Nov 10	LBT/MODS	1800s	1″2	T
PSO J142.3990−11.3604	2017 Mar 06	Magellan/LDSS3	900 s	1″0	F
PSO J148.4829+69.1812	2021 Dec 5	P200/DBSP	900 s	1″5	T
PSO J151.8186-16.1855	2017 May 15	Magellan/LDSS3	1200 s	1″0	F
	2018 Jun 4	Magellan/LDSS3	1200 s	1″0	
PSO J156.4466+38.9573	2021 Dec 5	P200/DBSP	400 s	1″5	T
PSO J158.6937−14.4210	2016 Nov 27	Keck/LRIS	900 s	1″0	F
PSO J169.1406+58.8894	2017 Apr 19	LBT/MODS	840 s	1″2	T
PSO J170.8326+20.2082	2022 June 13	Gemini-N/GMOS	1200 s	1″5	F
PSO J173.3198−06.9458	2017 Mar 06	Magellan/LDSS3	600 s	1″0	F
PSO J173.4601+48.2420	2021 May 12	LBT/MODS	4800s	1″2	F
PSO J175.4294+71.3236	2021 Dec 5	P200/DBSP	600 s	1″5	T
PSO J178.3733+28.5075	2021 Nov 30	P200/DBSP	600 s	1″5	T
PSO J182.3121+53.4633	2021 Dec 6	P200/DBSP	1500 s	1″5	T
PSO J193.3992−02.7820	2018 Jan 25	Magellan/LDSS3	900 s	1″0	T
PSO J196.3476+15.3899	2021 Dec 5	P200/DBSP	1200 s	1″5	T
PSO J197.8675+45.8040	2018 Jun 10	P200/DBSP	1800 s	1″5	T
PSO J207.5983+37.8099	2017 Apr 19	LBT/MODS	840 s	1″2	T
	2017 Apr 28	Keck/LRIS	1200s	1″0	
PSO J207.7780−21.1889	2017 Mar 06	Magellan/LDSS3	700 s	1″0	F
	2019 Jun 09	LBT/MODS	1800 s	1″2	
PSO J209.3825−08.7171	2017 Aug 08	Magellan/LDSS3	1200 s	1″0	T
PSO J215.4303+26.5325	2016 May 05	MMT/Red Channel	2400 s	1″0	F
PSO J218.3967+28.3306	2021 May 13	LBT/MODS	1800s	1″2	T
PSO J218.7714+04.8189	2021 Jul 13	P200/DBSP	3600 s	1″5	T
PSO J224.6506+10.2137	2022 Mar 6	Keck/LRIS	300 s	1″0	T
PSO J228.7029+01.3811	2021 Feb 19	VLT/FORS2	450 s	1″3	F
PSO J261.1247+37.3060	2022 Mar 6	Keck/LRIS	300 s	1″0	T
PSO J265.9298+41.4139	2017 Apr 19	LBT/MODS	840 s	1″2	T
PSO J271.4455+49.3067	2017 Apr 19	LBT/MODS	840 s	1″2	T
PSO J281.3361+53.7631	2020 Oct 22	LBT/MODS	1200s	1″2	T
PSO J288.6476+63.2479	2022 Sep 17	P200/DBSP	2400 s	1″5	T
PSO J306.3512−04.8227	2022 Sep 17	P200/DBSP	1320 s	1″5	T
PSO J307.7635−05.1958	2022 Sep 17	P200/DBSP	1290 s	1″5	T
PSO J334.0181−05.0048	2017 Sep 26	Magellan/LDSS3	1200 s	1″0	T
VIK J0046−2837	2014 Oct 28	VLT/FORS2	1362 s	1″3	F
VIK J0224−3435	2014 Nov 14	VLT/FORS2	1482 s	1″3	F
VIK J1152+0055	2014 Apr 30	VLT/FORS2	2615 s	1″3	F
VIK J2211−3206	2013 Dec 19	VLT/FORS2	1482 s	1″3	F
VIK J2227−3323	2015 Nov 05	VLT/FORS2	2600 s	1″3	F

Table 1
(Continued)

Quasar	Date	Telescope/Instrument	Exposure Time	Slit Width	QLF?
VIK J2315–2856	2015 Dec 10	VLT/FORS2	1500 s	1″3	F
VIK J2318–3029	2013 Dec 21	VLT/FORS2	1482 s	1″3	F

Note. The PS1 quasars are shown first, and the VIKING quasars are at the end of the table. For full coordinates and redshifts, see Table 2. The last column indicates whether the quasars are part of the $z \sim 6$ quasar luminosity function presented in Schindler et al. (2023).

We note that the $z \sim 6$ quasar luminosity function presented in Schindler et al. (2023) focuses on objects with $z_{P1} - y_{P1} < 0.5$, for which our spectroscopic follow-up has been more extensive.

2.2. VIKING Candidate Selection

The VIKING survey covers 1350 deg² of the sky in five bands $Z_{VI}YJHK_S$. The first requirement for our quasar selection is that the candidates need to be detected in at least the Z_{VI} and Y bands, but must be faint or not detected in the Kilo-Degree Survey (KiDS). KiDS is a public survey that covers almost the same area as VIKING, but in the optical Sloan $ugri$ bands (Kuijken et al. 2019). We then retained sources classified as point sources in the VIKING catalog (with a galaxy probability $P_{gal} < 0.95$; see Venemans et al. 2013 for details). To select quasar candidates in the redshift range $5.8 \lesssim z \lesssim 6.4$, we adopt the following criteria:

$$S/N(Z_{VI}) > 7$$
$$i - Z_{VI} > 2.2$$
$$Z_{VI} - Y < 1.0$$
$$-0.5 < Y - J < 0.5.$$

We performed forced photometry on the KiDS and VIKING pixel data to verify the catalog magnitudes and nondetections. All our candidates are visually inspected, and we use the fact that VIKING data are usually taken in different nights, including two epochs in J, to remove moving and variable objects. The locations of our discovered quasars in the $i_{forced} - Z_{VI}$ versus $Z_{VI} - Y$ plane are shown in the right panel of Figure 1.

2.3. Follow-up and Survey Photometry

We have compiled additional information from public surveys and obtained follow-up photometry for our quasar candidates. In some cases, this additional information was used to prioritize objects for spectroscopic follow-up. We also obtained follow-up photometry for quasars after their spectroscopic discovery to constrain their spectral energy distribution and secure absolute flux calibration for future near-infrared spectroscopic observations. In Table 3 we report follow-up photometry obtained in the following filters and telescopes: $I\#705$ (I_E) and $Z\#623$ (Z_E) with the ESO Faint Object Spectrograph and Camera (EFOSC2; Snodgrass et al. 2008) at the NTT telescope in La Silla, J_G and H_G with the GROND camera (Greiner et al. 2008) at the MPG 2.2 m telescope in La Silla, $J_SH_SK_S$ with SOFI (Moorwood et al. 1998) at the NTT telescope in La Silla, and Y_R with the RetroCam[18] camera at the Du Pont telescope in Las Campanas Observatory.

We report the photometry and observation dates in Table 3. For completeness, in Table 3 we also report $IZYHK$ magnitudes from public surveys or published papers when available. The public surveys are DELS (Dey et al. 2019), DES (Abbott et al. 2018, 2021), KiDS (Kuijken et al. 2019), UHS (Dye et al. 2018), UKIDSS (Lawrence et al. 2007), VHS (McMahon et al. 2013), and VIKING (Edge et al. 2013).

Finally, we note that most of our VIKING-selected candidates were followed-up with EFOSC2 observations in the I_E band. Sources that satisfied $I_E - Z_{VI} > 1.0$ were considered high priority for spectroscopic follow-up.

3. Discovery of 55 Quasars

3.1. Spectroscopic Observations

Here we present the discovery of 55 quasars: 48 selected from Pan-STARRS1, and 7 from VIKING (see Section 2). We note that 2 of the 3 VIKING quasars with Pan-STARRS1 information satisfy all of our Pan-STARRS1 selection criteria except for $S/N(z_{P1}) > 10$ (8.8 and 9.0 for J0046–2837 and J2315–2856, respectively). J2318–3029, on the other hand, would have been rejected by three criteria: low $S/N(z_{P1}) = 6.1$, classified as extended in both z_{P1} and y_{P1}, and its y_{P1} band was flagged because its moments were not measured because the S/N was low (flag MOMENTS_SN = 0x00040000). This shows that further Pan-STARRS1 quasars could be found by relaxing the criteria from Section 2.1. Indeed, we did find two quasars by loosening some of the criteria. In one case, the selection was enabled by requiring radio emission, as discussed in Section 3.8.

The discovery of the 55 quasars presented in this work has been a large effort, involving multiple observatories in the time frame 2013 November 19–2022 September 28. Five of these quasars have been independently discovered by other groups: P158–14 by Chehade et al. (2018), P173+48 and P207+37 by Gloudemans et al. (2022), and P127+26 by S. Warren et al. 2023, in preparation. A few of these quasars have been part of multiple follow-up campaigns, and some of their properties have been presented in the literature (e.g., Decarli et al. 2018; Eilers et al. 2020; Venemans et al. 2020; Bischetti et al. 2022). These quasars are discussed in Section 3.3. The spectroscopic observations log is listed in Table 1, and the main quasar properties are presented in Table 2. Multiple observations for the quasars in Table 1 were required because the first spectrum had low quality or was taken under very poor weather conditions, and the quasars were followed-up later on. The latest spectra are shown in Figure 2.

The spectrographs/telescopes used for the discovery of these quasars are the Double Spectrograph (DBSP; Oke & Gunn 1982) on the 200 inch (5 m) Hale telescope at Palomar Observatory (P200), the Low Dispersion Survey Spectrograph (LDSS3; Stevenson et al. 2016) at the Clay Magellan telescope

---

[18] http://www.lco.cl/?epkb_post_type_1 = retrocam-specs

Table 2
Properties of the Quasars Discovered in This Work, Sorted by R.A.

Quasar	R.A. ICRS	Decl. ICRS	z	z-method	z reference	m_{1450} mag	M_{1450} mag	m_{2500} mag	Best Template	Notes
P000−04	00:00:09.99	−04:16:26.05	5.77	template	1	20.79	−25.84	21.33	weak-Lyα	
P000−18	00:00:19.33	−18:14:09.64	5.9	template	1	21.48	−25.19	22.02	strong-Lyα	
P001−28	00:06:45.36	−28:40:42.05	5.95	template	1	21.07	−25.61	21.75	selsing2016	
P002+03	00:10:10.30	+03:03:47.57	5.64	template	1	20.92	−25.67	21.46	weak-Lyα	low S/N-BAL
P008+10	00:34:26.00	+10:51:06.70	5.98	template	1	20.62	−26.07	21.16	yang2021	
J0046−2837	00:46:23.65	−28:37:47.68	6.02	template	1	21.34	−25.36	21.88	yang2021	
P017−11	01:08:16.60	−11:59:31.00	5.8	template	1	20.70	−25.94	21.31	strong-Lyα	
P030−17	02:00:33.30	−17:37:26.00	6.09	template	1	21.36	−25.36	21.90	strong-Lyα	
P032−17	02:11:40.52	−17:04:28.74	5.99	template	1	20.89	−25.80	21.43	weak-Lyα	
J0224−3435	02:24:56.75	−34:35:23.00	5.78	template	1	21.77	−24.86	22.31	weak-Lyα	
P038−18	02:32:45.94	−18:34:24.61	5.68	template	1	20.57	−26.04	21.11	weak-Lyα	
P043−02	02:52:26.68	−02:37:20.70	6.17	template	1	21.05	−25.69	21.72	vandenberk2001	
P050−18	03:22:14.54	−18:41:17.43	6.09	template	1	20.45	−26.27	20.99	weak-Lyα	radio-loud
P065+01	04:23:50.15	+01:43:24.73	5.79	template	1	20.08	−26.56	20.62	weak-Lyα	BAL
P072−07	04:50:19.81	−07:53:30.59	5.75	template	1	20.97	−25.66	21.51	strong-Lyα	
P076−10	05:04:56.27	−10:53:16.09	5.93	template	1	20.55	−26.13	21.09	weak-Lyα	
P119+02	07:56:22.38	+02:18:20.16	5.73	template	1	20.42	−26.20	20.96	weak-Lyα	
P124+12	08:16:00.79	+12:59:56.31	5.8	template	1	21.05	−25.59	21.59	median-Lyα	
P127+26	08:28:13.41	+26:33:55.49	6.14	template	1	20.52	−26.21	21.06	median-Lyα	
P142−11	09:29:35.77	−11:21:37.59	5.61	template	1	20.60	−25.99	21.14	weak-Lyα	
P148+69	09:53:55.90	+69:10:52.62	5.84	template	1	20.19	−26.46	20.73	weak-Lyα	
P151−16	10:07:16.49	−16:11:07.94	5.84	template	1	21.45	−25.20	22.12	vandenberk2001	
P156+38	10:25:47.19	+38:57:26.30	5.75	template	1	19.85	−26.78	20.39	strong-Lyα	
P158−14	10:34:46.51	−14:25:15.85	6.0685	[C II]	3	19.39	−27.32	19.93	median-Lyα	
P169+58	11:16:33.76	+58:53:22.19	5.73	template	1	20.59	−26.03	21.13	median-Lyα	
P170+20	11:23:19.84	+20:12:29.79	6.41	template	1	20.70	−26.10	21.24	yang2021	lensed?
P173−06	11:33:16.78	−06:56:44.85	5.77	template	1	20.66	−25.97	21.20	strong-Lyα	BAL
P173+48	11:33:50.44	+48:14:31.21	6.233	absorption	1	21.63	−25.12	22.17	strong-Lyα	radio-loud
P175+71	11:41:43.07	+71:19:25.03	5.86	template	1	20.71	−25.95	21.25	yang2021	
J1152+0055	11:52:21.27	+00:55:36.69	6.3643	[C II]	2	21.74	−25.05	22.41	vandenberk2001	
P178+28	11:53:29.60	+28:30:27.11	5.68	template	1	19.84	−26.77	20.38	weak-Lyα	
P182+53	12:09:14.93	+53:27:48.05	5.99	template	1	21.05	−25.64	21.58	yang2021	radio-loud
P193−02	12:53:35.82	−02:46:55.29	5.8	template	1	21.21	−25.43	21.75	median-Lyα	radio-loud
P196+15	13:05:23.43	+15:23:23.68	5.69	template	1	20.44	−26.17	20.98	weak-Lyα	low S/N
P197+45	13:11:28.20	+45:48:14.69	5.66	template	1	20.87	−25.73	21.41	weak-Lyα	low S/N
P207+37	13:50:23.60	+37:48:35.67	5.69	template	1	20.76	−25.85	21.29	weak-Lyα	radio-loud
P207−21	13:51:06.72	−21:11:20.27	5.81	template	1	20.69	−25.95	21.23	strong-Lyα	BAL
P209−08	13:57:31.82	−08:43:01.74	5.77	template	1	21.44	−25.19	21.98	strong-Lyα	
P215+26	14:21:43.29	+26:31:57.14	6.28	template	1	20.40	−26.37	20.94	strong-Lyα	BAL
P218+28	14:33:35.22	+28:19:50.60	5.91	template	1	20.82	−25.85	21.36	median-Lyα	
P218+04	14:35:05.15	+04:49:08.32	6.14	template	1	20.83	−25.90	21.50	vandenberk2001	BAL
P224+10	14:58:36.16	+10:12:49.67	5.6	template	1	19.68	−26.90	20.22	weak-Lyα	BAL
P228+01	15:14:48.70	+01:22:52.25	5.76	template	1	21.38	−25.25	22.05	selsing2016	
P261+37	17:24:29.94	+37:18:21.80	5.76	template	1	21.03	−25.60	21.70	vandenberk2001	
P265+41	17:43:43.15	+41:24:50.22	6.0263	[C II]	3	20.76	−25.94	21.29	yang2021	BAL
P271+49	18:05:46.93	+49:18:24.23	5.74	template	1	20.38	−26.24	21.05	vandenberk2001	
P281+53	18:45:20.68	+53:45:47.34	6.18	template	1	20.09	−26.65	20.63	strong-Lyα	BAL
P288+63	19:14:35.44	+63:14:52.54	5.96	template	1	20.64	−26.04	21.18	yang2021	
P306−04	20:25:24.31	−04:49:21.88	5.84	template	1	20.71	−25.94	21.25	yang2021	
P307−05	20:31:03.26	−05:11:45.20	5.8	template	1	20.86	−25.78	21.53	vandenberk2001	
J2211−3206	22:11:12.39	−32:06:12.95	6.3394	[C II]	2	18.78	−28.00	19.45	strong-Lyα	BAL
P334−05	22:16:04.36	−05:00:17.58	6.15	template	1	21.07	−25.66	21.61	median-Lyα	
J2227−3323	22:27:18.58	−33:23:35.02	6.12	template	1	21.32	−25.41	21.86	weak-Lyα	
J2315−2856	23:15:07.39	−28:56:17.40	5.89	template	1	21.31	−25.35	21.85	strong-Lyα	
J2318−3029	23:18:33.10	−30:29:33.36	6.1456	[C II]	4	20.34	−26.39	20.88	median-Lyα	

References. (1) This work, (2) Decarli et al. (2018), (3) Eilers et al. (2020), (4) Venemans et al. (2020).
Note. The typical redshift uncertainties for estimates based on the z-method = template is <0.03 (see Section 3.2).

(This table is available in machine-readable form.)

Table 3
Photometry of the Quasars Discovered in This Work, Sorted by R.A.

Quasar	$g_{\rm P1}$ mag	$r_{\rm P1}$ mag	$i_{\rm P1}$ mag	$z_{\rm P1}$ mag	$y_{\rm P1}$ mag	I mag	$I_{\rm ref}$	Z mag	$Z_{\rm ref}$	Y mag	$Y_{\rm ref}$	J mag	$J_{\rm ref}$	H mag	$H_{\rm ref}$	K mag	$K_{\rm ref}$
P000−04	>23.84	>23.44	>23.92	20.70 ± 0.06	20.50 ± 0.11	⋯	⋯	20.74 ± 0.01	18	20.74 ± 0.25	22	20.35 ± 0.19	22	⋯	⋯	⋯	⋯
P000−18	>23.82	>23.75	23.54 ± 0.34	21.09 ± 0.07	21.02 ± 0.17	23.24 ± 0.18	8	⋯	⋯	21.36 ± 0.26	22	21.32 ± 0.15	11	⋯	⋯	⋯	⋯
P001−28	>23.49	>23.67	>23.42	21.03 ± 0.07	21.17 ± 0.19	⋯	⋯	⋯	⋯	⋯	⋯	21.47 ± 0.11	15	21.31 ± 0.15	15	⋯	⋯
P002+03	>23.79	>23.78	23.05 ± 0.22	20.83 ± 0.07	20.89 ± 0.16	21.90 ± 0.04	17	21.08 ± 0.02	18	20.84 ± 0.18	21	19.97 ± 0.11	21	19.30 ± 0.08	21	19.21 ± 0.07	21
P008+10	>23.56	>23.53	22.80 ± 0.25	20.74 ± 0.07	20.38 ± 0.10	⋯	⋯	20.34 ± 0.02	18	20.28 ± 0.05	16	20.22 ± 0.14	21	20.12 ± 0.19	21	19.94 ± 0.18	21
J0046−2837	>23.88	>23.44	>23.70	21.47 ± 0.12	21.01 ± 0.19	23.65 ± 0.06	3	21.44 ± 0.06	23	21.25 ± 0.11	23	20.92 ± 0.08	23	20.66 ± 0.09	23	20.24 ± 0.09	23
P017−11	>23.81	>23.55	23.19 ± 0.27	20.97 ± 0.07	20.82 ± 0.15	22.02 ± 0.10	7	21.20 ± 0.09	6	21.15 ± 0.08	16	21.13 ± 0.16	9	⋯	⋯	⋯	⋯
P030−17	>23.66	>23.07	23.51 ± 0.26	21.29 ± 0.12	20.84 ± 0.19	23.38 ± 0.14	17	20.94 ± 0.01	18	21.21 ± 0.13	17	21.00 ± 0.15	22	⋯	⋯	⋯	⋯
P032−17	>23.69	>23.49	23.33 ± 0.25	21.23 ± 0.08	20.77 ± 0.14	23.47 ± 0.14	17	20.65 ± 0.01	18	20.53 ± 0.08	17	20.52 ± 0.09	22	⋯	⋯	20.00 ± 0.16	22
J0224−3435	⋯	⋯	>24.23	⋯	⋯	23.08 ± 0.11	4	21.78 ± 0.08	23	21.79 ± 0.15	23	21.73 ± 0.16	23	21.53 ± 0.34	23	21.11 ± 0.26	23
P038−18	>23.69	>23.49	22.70 ± 0.14	20.57 ± 0.05	20.44 ± 0.10	21.53 ± 0.03	17	20.43 ± 0.01	18	20.47 ± 0.09	17	20.27 ± 0.10	22	⋯	⋯	20.29 ± 0.28	22
P043−02	>23.51	>23.80	>23.80	21.27 ± 0.07	20.69 ± 0.12	>24.41	17	21.08 ± 0.02	18	21.15 ± 0.12	17	20.86 ± 0.15	22	⋯	⋯	⋯	⋯
P050−18	>23.89	>23.34	>23.66	21.19 ± 0.08	20.68 ± 0.13	24.05 ± 0.33	17	20.89 ± 0.02	18	20.79 ± 0.08	16	20.59 ± 0.09	22	20.21 ± 0.16	10	20.60 ± 0.27	22
P065+01	>23.32	>23.28	22.72 ± 0.21	20.43 ± 0.06	20.09 ± 0.08	⋯	⋯	20.39 ± 0.02	18	⋯	⋯	19.74 ± 0.05	24	⋯	⋯	19.37 ± 0.05	13
P072−07	>23.70	>23.67	23.11 ± 0.21	20.75 ± 0.08	20.92 ± 0.14	⋯	⋯	21.43 ± 0.03	18	⋯	⋯	⋯	⋯	⋯	⋯	⋯	⋯
P076−10	>23.43	>23.48	>22.91	20.73 ± 0.05	20.67 ± 0.13	⋯	⋯	⋯	⋯	⋯	⋯	20.37 ± 0.17	22	⋯	⋯	19.78 ± 0.22	22
P119+02	>23.96	>23.78	22.59 ± 0.14	20.44 ± 0.04	20.27 ± 0.08	⋯	⋯	20.48 ± 0.04	18	⋯	⋯	19.96 ± 0.08	10	19.60 ± 0.13	10	⋯	⋯
P124+12	>23.44	>23.68	23.26 ± 0.28	20.80 ± 0.05	21.20 ± 0.15	⋯	⋯	20.96 ± 0.02	18	⋯	⋯	⋯	⋯	⋯	⋯	⋯	⋯
P127+26	>23.74	>23.73	>23.44	20.72 ± 0.06	20.42 ± 0.10	⋯	⋯	20.38 ± 0.02	18	20.60 ± 0.05	25	20.53 ± 0.06	25	20.36 ± 0.25	25	20.08 ± 0.17	25
P142−11	>23.66	>23.57	22.67 ± 0.16	20.64 ± 0.05	20.55 ± 0.08	⋯	⋯	20.63 ± 0.04	18	⋯	⋯	⋯	⋯	⋯	⋯	19.83 ± 0.08	14
P148+69	>23.31	>23.11	22.98 ± 0.28	20.37 ± 0.05	20.32 ± 0.15	⋯	⋯	20.29 ± 0.01	18	⋯	⋯	⋯	⋯	⋯	⋯	⋯	⋯
P151−16	>23.31	>23.38	>23.31	21.24 ± 0.08	21.21 ± 0.15	⋯	⋯	⋯	⋯	21.11 ± 0.22	22	20.91 ± 0.24	22	⋯	⋯	⋯	⋯
P156+38	>23.53	23.64 ± 0.30	22.14 ± 0.06	19.84 ± 0.02	19.94 ± 0.08	⋯	⋯	20.32 ± 0.01	18	⋯	⋯	20.12 ± 0.12	20	⋯	⋯	⋯	⋯
P158−14	>22.50	>23.05	22.25 ± 0.25	19.57 ± 0.02	19.28 ± 0.04	⋯	⋯	⋯	⋯	19.28 ± 0.07	25	19.25 ± 0.08	25	19.15 ± 0.10	25	18.68 ± 0.09	25
P169+58	>22.94	>23.51	22.65 ± 0.17	20.46 ± 0.06	20.82 ± 0.20	⋯	⋯	20.74 ± 0.02	18	⋯	⋯	⋯	⋯	⋯	⋯	⋯	⋯
P170+20	>23.74	22.95 ± 0.19	22.43 ± 0.29	20.38 ± 0.03	20.17 ± 0.06	⋯	⋯	20.31 ± 0.02	18	⋯	⋯	19.85 ± 0.11	20	⋯	⋯	⋯	⋯
P173−06	>23.70	>23.91	22.89 ± 0.20	20.43 ± 0.05	20.86 ± 0.12	⋯	⋯	20.78 ± 0.02	18	20.76 ± 0.20	22	20.30 ± 0.13	22	20.12 ± 0.15	22	20.08 ± 0.25	22
P173+48	>24.24	>23.82	>23.78	21.59 ± 0.10	21.81 ± 0.29	⋯	⋯	21.34 ± 0.03	18	⋯	⋯	⋯	⋯	⋯	⋯	⋯	⋯
P175+71	>23.40	>23.24	23.19 ± 0.31	20.28 ± 0.04	20.57 ± 0.12	⋯	⋯	20.58 ± 0.02	18	⋯	⋯	⋯	⋯	⋯	⋯	⋯	⋯
J1152+0055	⋯	⋯	>24.37	⋯	⋯	>24.39	2	22.12 ± 0.14	23	21.57 ± 0.17	23	21.64 ± 0.23	23	21.53 ± 0.35	23	21.29 ± 0.30	23
P178+28	>23.66	>23.91	21.95 ± 0.08	19.83 ± 0.03	19.82 ± 0.06	⋯	⋯	20.01 ± 0.02	18	⋯	⋯	19.63 ± 0.09	20	⋯	⋯	⋯	⋯
P182+53	>24.11	>23.95	>23.62	21.16 ± 0.07	20.89 ± 0.13	⋯	⋯	20.89 ± 0.03	18	⋯	⋯	⋯	⋯	⋯	⋯	⋯	⋯
P193−02	>24.04	>24.03	23.23 ± 0.28	21.14 ± 0.07	21.15 ± 0.12	⋯	⋯	21.07 ± 0.03	18	20.88 ± 0.19	21	20.63 ± 0.17	21	20.68 ± 0.20	21	⋯	⋯
P196+15	>23.77	>23.66	23.43 ± 0.28	20.58 ± 0.06	20.54 ± 0.12	⋯	⋯	20.86 ± 0.02	18	20.68 ± 0.14	21	20.56 ± 0.17	21	⋯	⋯	19.69 ± 0.14	21
P197+45	>23.99	>23.88	23.29 ± 0.25	20.88 ± 0.05	20.81 ± 0.12	⋯	⋯	20.65 ± 0.02	18	⋯	⋯	20.29 ± 0.18	20	⋯	⋯	⋯	⋯
P207+37	>23.92	>23.45	23.29 ± 0.27	20.83 ± 0.05	20.57 ± 0.09	⋯	⋯	20.72 ± 0.02	18	⋯	⋯	20.37 ± 0.17	20	⋯	⋯	⋯	⋯
P207−21	>23.42	>23.58	>23.56	20.62 ± 0.05	20.72 ± 0.16	⋯	⋯	⋯	⋯	20.48 ± 0.13	22	20.54 ± 0.19	22	⋯	⋯	20.01 ± 0.23	22
P209−08	>23.94	>23.55	>23.55	21.10 ± 0.06	21.41 ± 0.17	⋯	⋯	21.50 ± 0.07	18	⋯	⋯	⋯	⋯	⋯	⋯	⋯	⋯
P215+26	>23.83	>23.83	>23.93	21.12 ± 0.06	20.43 ± 0.08	⋯	⋯	20.60 ± 0.03	18	⋯	⋯	20.40 ± 0.16	20	⋯	⋯	⋯	⋯
P218+28	>23.88	>23.55	23.29 ± 0.33	20.81 ± 0.06	20.63 ± 0.13	⋯	⋯	20.60 ± 0.02	18	⋯	⋯	20.13 ± 0.17	20	⋯	⋯	⋯	⋯
P218+04	>23.85	>23.86	23.30 ± 0.31	20.98 ± 0.06	20.57 ± 0.10	⋯	⋯	20.88 ± 0.03	18	20.98 ± 0.21	21	21.04 ± 0.33	21	⋯	⋯	⋯	⋯
P224+10	>24.09	23.71 ± 0.31	21.87 ± 0.08	19.88 ± 0.02	19.80 ± 0.04	⋯	⋯	19.90 ± 0.01	18	19.82 ± 0.07	21	19.23 ± 0.06	20	19.02 ± 0.06	21	18.93 ± 0.05	21
P228+01	>23.83	>23.67	23.26 ± 0.25	21.20 ± 0.06	21.10 ± 0.18	⋯	⋯	21.79 ± 0.08	18	⋯	⋯	21.94 ± 0.13	12	⋯	⋯	⋯	⋯
P261+37	>23.64	>23.78	23.36 ± 0.18	20.87 ± 0.06	20.61 ± 0.09	⋯	⋯	21.12 ± 0.03	18	⋯	⋯	⋯	⋯	⋯	⋯	⋯	⋯
P265+41	>23.57	>23.95	>24.25	20.83 ± 0.06	21.17 ± 0.15	⋯	⋯	20.45 ± 0.01	18	⋯	⋯	20.30 ± 0.16	20	⋯	⋯	⋯	⋯
P271+49	>23.75	>23.89	22.84 ± 0.15	20.19 ± 0.04	20.56 ± 0.10	⋯	⋯	20.59 ± 0.02	18	⋯	⋯	20.26 ± 0.18	20	⋯	⋯	⋯	⋯
P281+53	>23.77	>23.64	23.88 ± 0.35	20.17 ± 0.03	20.25 ± 0.10	⋯	⋯	19.90 ± 0.01	18	⋯	⋯	19.72 ± 0.11	20	⋯	⋯	⋯	⋯
P288+63	>23.81	>23.40	23.27 ± 0.27	20.68 ± 0.06	20.76 ± 0.15	⋯	⋯	20.59 ± 0.03	18	⋯	⋯	⋯	⋯	⋯	⋯	⋯	⋯
P306-04	>23.76	>23.54	22.63 ± 0.13	20.53 ± 0.05	20.64 ± 0.14	⋯	⋯	20.79 ± 0.04	18	⋯	⋯	⋯	⋯	⋯	⋯	⋯	⋯
P307−05	>23.66	>23.77	>23.85	20.53 ± 0.06	21.01 ± 0.17	⋯	⋯	20.90 ± 0.03	18	⋯	⋯	20.75 ± 0.23	22	⋯	⋯	⋯	⋯
J2211−3206	⋯	⋯	>24.26	⋯	⋯	>23.71	19	19.91 ± 0.02	23	19.85 ± 0.03	23	19.62 ± 0.03	23	19.38 ± 0.05	23	19.00 ± 0.03	23
P334−05	>23.77	>23.67	>23.89	21.53 ± 0.11	21.04 ± 0.19	⋯	⋯	21.38 ± 0.04	18	⋯	⋯	20.71 ± 0.23	22	⋯	⋯	⋯	⋯
J2227−3323	⋯	⋯	>24.50	⋯	⋯	24.09 ± 0.36	5	21.91 ± 0.11	23	21.43 ± 0.15	23	21.62 ± 0.20	23	21.28 ± 0.22	23	21.25 ± 0.24	23

Table 3
(Continued)

Quasar	g_{P1} mag	r_{P1} mag	i_{P1} mag	z_{P1} mag	y_{P1} mag	I mag	I_{ref}	Z mag	Z_{ref}	Y mag	Y_{ref}	J mag	J_{ref}	H mag	H_{ref}	K mag	K_{ref}
J2315–2856	>23.70	>23.32	23.66 ± 0.27	21.26 ± 0.12	21.15 ± 0.21	22.29 ± 0.09	5	21.20 ± 0.06	23	21.23 ± 0.14	23	21.09 ± 0.12	23	20.95 ± 0.15	23	20.53 ± 0.11	23
J2318–3029	>23.24	>22.73	>24.19	20.66 ± 0.18	20.08 ± 0.14	22.33 ± 0.09	1	20.58 ± 0.04	23	20.58 ± 0.08	23	20.20 ± 0.06	23	20.00 ± 0.06	23	19.69 ± 0.06	23

References. (1) EFOSC2 2013-09-28, (2) EFOSC2 2014-03-03, (3) EFOSC2 2014-07-24, (4) EFOSC2 2014-07-27, (5) EFOSC2 2015-07-22, (6) EFOSC2 2016-09-13, (7) EFOSC2 2016-09-14, (8) EFOSC2 2018-06-26, (9) GROND 2016-09-22, (10) GROND 2017-01-01, (11) SOFI 2017-05-29, (12) SOFI 2018-06-26, (13) SOFI 2019-12-13, (14) SOFI 2019-12-14, (15) SOFI 2020-11-20, (16) Retrocam 2016-09-20, (17) DES DR2, (18) DELS DR9, (19) KiDS, (20) UHS, (21) UKIDSS, (22) VHS, (23) VIKING, (24) Bischetti et al. (2022), (25) Ross & Cross (2020).

Note. The PS1 magnitudes are dereddened. Reddened magnitudes can be obtained by adding $\lambda_f \times E(B - V)$ with $\lambda_f = (3.172, 2.271, 1.682, 1.322, 1.087)$ for $(g_{P1}, r_{P1}, i_{P1}, z_{P1}, y_{P1})$; see Schlafly & Finkbeiner (2011). For the VIKING quasars, the magntides reported in the i_{P1} column are actually i magnitudes from the KiDS survey. Limits are reported at 3σ.

(This table is available in machine-readable form.)
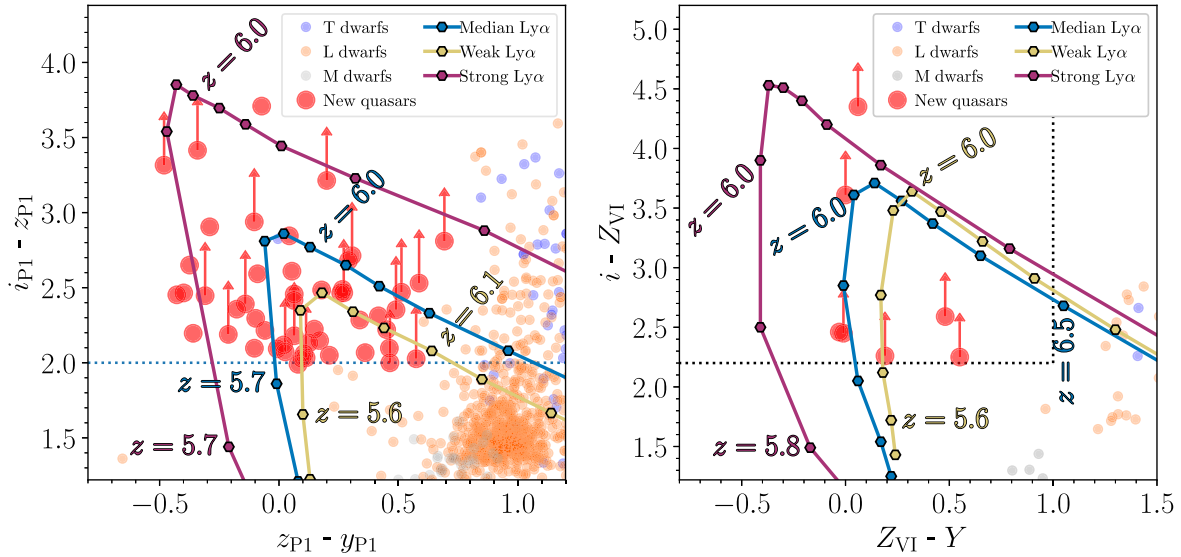
Figure 1. Left: $i_{P1} - z_{P1}$ vs. $z_{P1} - y_{P1}$ diagram showing the main Pan-STARRS1 color criteria, the location of the discovered quasars (red circles), and the compilation of *MLT* dwarfs from Bañados et al. (2016). The solid lines represent the color tracks of the $z \sim 6$ quasar composites with a strong, median, and weak Lyα line from Bañados et al. (2016). The symbols are plotted in steps of $\Delta z = 0.1$, and two redshifts are labeled for each track. Note that the four VIKING quasars without PS1 information are not shown here (see Table 3). Right: Same as for the left panel, but for the $i - Z_{VI}$ vs. $Z_{VI} - Y$ diagram, showing the main KiDS-VIKING color criteria and the location of the discovered quasars.
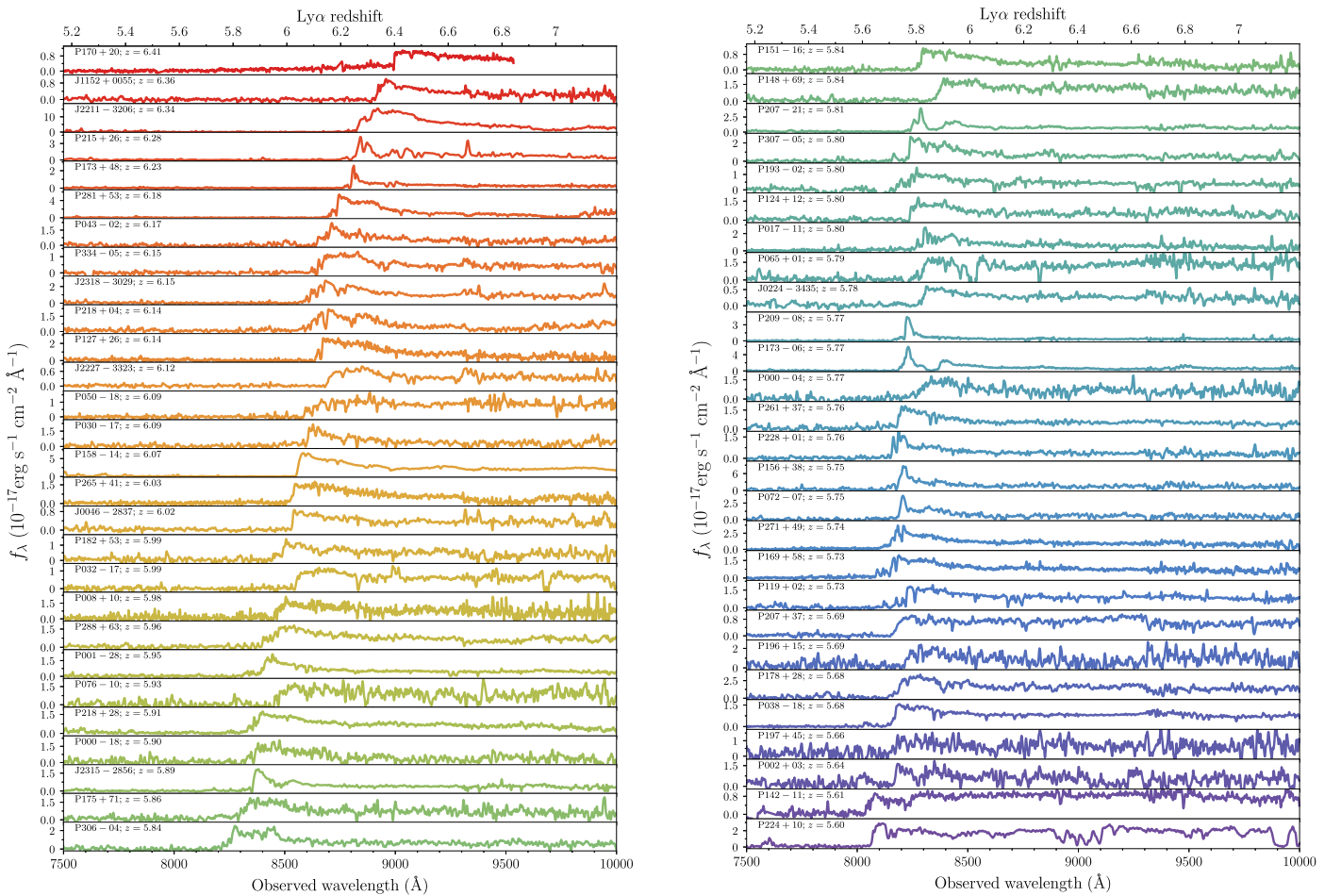
Figure 2. Discovery spectra of the 55 $z \sim 6$ quasars presented in this work, sorted by decreasing redshift.

at Las Campanas Observatory, the Multi-Object Double Spectrograph (MODS; Pogge et al. 2010) at the Large Binocular Telescope (LBT), EFOSC2 at the NTT telescope in La Silla, the Low Resolution Imaging Spectrometer (LRIS; Oke et al. 1995) at the Keck telescope on Maunakea, the Gemini Multi-Object Spectrographs (GMOS; Hook et al. 2004) on the Gemini-North telescope, the Red Channel Spectrograph (Schmidt et al. 1989) on the 6.5 m MMT Telescope, and the

FOcal Reducer/low dispersion Spectrograph 2 (FORS2; Appenzeller & Rupprecht 1992) at the Very Large Telescope (VLT).

The spectra were reduced with standard procedures, including bias subtraction, flat-fielding, sky subtraction, extraction, and wavelength and flux calibration. All observations taken before 2020 were reduced with the Image Reduction and Analysis Facility (IRAF; Tody 1986). Observations taken after 2020 were reduced with the Python Spectroscopic Data Reduction Pipeline (PypeIt; Prochaska et al. 2020a, 2020b), except for the P200/DBSP, which were reduced with IRAF and NTT/EFOSC2 data that were reduced with the EsoReflex pipeline (Freudling et al. 2013). The spectra were absolute flux calibrated by matching the spectra to their z_{P1} magnitude (or Z_{VI} when no z_{P1} exists). The 55 spectra sorted by descending redshift are shown in Figure 2.

3.2. Redshifts and Continuum Magnitudes

Different Lyα profiles can significantly impact quasar colors and expected redshifts. From the colors of the quasars shown in Figure 1, we expect a significant fraction to have weak or median Lyα, and only a few to have strong emission lines.

To estimate the redshifts, we fit the spectra of the quasars with six different quasar templates to encompass an extensive range of emission line properties (especially Lyα). The six templates are:

1. *vandenberk2001*, which is the median of more than 2000 quasar spectra from the Sloan Digital Sky Survey (Vanden Berk et al. 2001).
2. *selsing2016*, which is the median of seven bright $1 < z < 2$ quasars (Selsing et al. 2016).
3. *yang2021*, which is the median spectra of 38 $z > 6.5$ quasars, as presented in Yang et al. (2021).
4. *median*-Lyα, which is the median of 117 $z \sim 6$ quasars from Bañados et al. (2016).
5. *strong*-Lyα, which is the median of the 10% of the $z \sim 6$ spectra with the largest rest-frame equivalent width (Lyα + N v) from Bañados et al. (2016).
6. *weak*-Lyα, which is the median of the 10% of the $z \sim 6$ spectra with the smallest rest-frame equivalent width (Lyα + N v) from Bañados et al. (2016).

The Lyα profiles of (iii) and (iv) are very similar. The templates (iv)–(vi) only cover up to 1400 Å. We stitch them at a rest-frame wavelength 1300 Å with the *yang2021* template so that we can use the best-fitting templates to also derive rest-frame magnitudes.

After masking prominent absorption features, we choose the best-fitting template with the minimum χ^2 in the 1212–1400 Å wavelength range. This procedure works well for most cases, but it has a few exceptions. The most common case of quasars that are not well fit are those with narrow Lyα and N v lines that are not represented in our templates. For most of the quasars that are not well fit, the strength of the Lyα line is between the median-Lyα templates and strong-Lyα (quasars P000–18, P030–17, P072–07, P156+38, P173–06, P173+48, P207–21, and J2315–2856). The next common cases are broad absorption line (BAL) quasars with narrow N v and highly absorbed Lyα (quasars P215+26, P281+53, J2211–3206). In all the cases discussed above, the strong-Lyα template gives a clearly superior fit (visually) even if it does not provide the smallest χ^2. This is because the strong-Lyα template is the only

one that includes a prominent narrow N V line. We report the values derived using the strong-Lyα template in all these cases. P170+20 is the other exception and is discussed further in Section 3.3.

To quantify the uncertainty in our redshift estimates, we proceeded as follows. We compiled a list of published Mg II and [C II] redshifts for $z \gtrsim 6$ quasars for which the discovery spectra were available (i.e., of similar quality to the spectra analyzed in this paper). This resulted in 39 quasars with Mg II redshifts (from Mazzucchelli et al. 2017b; Onoue et al. 2019; Shen et al. 2019; Schindler et al. 2020) and 27 quasars with [C II] redshifts (from Wang et al. 2011, 2013; Mazzucchelli et al. 2017b; Decarli et al. 2018; Eilers et al. 2020; Venemans et al. 2020; Meyer et al. 2022). We then calculated the difference between these redshifts and the template fitting redshifts for these quasars. The mean difference and standard deviation are -0.01 ± 0.02 and $+0.01 \pm 0.03$ for the $z_{Mgii} - z_{temp}$ and $z_{[Cii]} - z_{temp}$, respectively. Therefore, the typical uncertainties in our redshift estimates are <0.03.

Table 2 lists the measured redshifts, rest-frame magnitudes at 1450 Å, and the best-fit templates used to derive the rest-frame magnitudes and, in most cases, the redshifts. If [C II] redshifts are available, we use those values (Decarli et al. 2018; Eilers et al. 2020; Venemans et al. 2020). In one case (P173+48), we use an absorption feature to determine the redshift (see Section 3.8).

3.3. Notes on Selected Objects

Here we present additional notes on selected objects, sorted by R.A.

3.3.1. VIK J0046–2837 (z = 6.02)

ALMA observations for this quasar were presented in Decarli et al. (2018), finding a faint cold dust continuum detection and no [C II] line. Schindler et al. (2020) report a Mg II redshift of $z = 5.993 \pm 0.002$, and Farina et al. (2022) estimate a black hole mass of $M_{BH} = 3.5 \times 10^8 \, M_\odot$.

3.3.2. PSO J065.9589+01.7235 (z = 5.79)

PSO J065.9589+01.7235 had $z_{P1} - y_{P1} = 0.6$ in PV2 and is therefore not part of the luminosity function presented in Schindler et al. (2023). However, its color in the latest version of PS1 is $z_{P1} - y_{P1} = 0.34$, and it would have been selected. This quasar is also part of the XQR-30 sample (V. D'Odorico et al. 2023, in preparation; https://xqr30.inaf.it) and it was classified as a BAL quasar by Bischetti et al. (2022). Our template redshift of $z = 5.79$ is consistent with the Mg II redshift $z = 5.804$ reported by Bischetti et al. (2022).

3.3.3. PSO J127.0558+26.5654 (z = 6.14)

This quasar is also known as J0828+2633 (S. Warren et al. 2023, in preparation). It has been reported and studied in other published work (e.g., Mortlock et al. 2012; Ross & Cross 2020), and an actual optical spectrum was first shown in Li et al. (2020). Our redshift estimate derived from template fitting ($z = 6.14$) is significantly different to the redshift used in the literature of $z = 6.05$, which is only possible if the Lyα emission were completely absorbed. For completeness, the redshift derived using our weak-Lyα template is $z = 6.08$.

3.3.4. PSO J148.4829+69.1812 (z = 5.84)

This quasar is located in the outskirts of M81, and therefore myriad multiwavelength data in the field already exist. Furthermore, its location is suitable for parallel observations with JWST covering both the quasar field and M81. The Lyα line is weak or heavily absorbed. The detailed spectral energy distribution and environment studies of this source will be presented in a separate paper.

3.3.5. PSO J158.6937–14.4210 (z = 6.0685)

This quasar was independently discovered by Chehade et al. (2018), and it has appeared in a number of other articles (e.g., Eilers et al. 2020; Schindler et al. 2020). Eilers et al. (2020) measure a very small proximity zone and classify this source as a "young quasar". Our best-fitting template is a median-Lyα yielding $z = 6.06$, in good agreement with $z = 6.0685 \pm 0.0001$ as measured from the [C II] line from the host galaxy (Eilers et al. 2020). To measure the rest-frame magnitudes, we use the median-Lyα template at the [C II] redshift.

3.4. PSO J170.8326+20.2082 (z = 6.41)

This quasar shows the most peculiar spectrum in the sample. We show postage stamps and 1D and 2D spectra of this quasar in Figure 3. There is an extremely sharp break in flux at 8992 Å, consistent with a $z \sim 6.4$ quasar. Such a high redshift is at odds with its blue $z_{P1} - y_{P1} < 0$ color (see Section 2.1). An excess of flux blueward of the break explains the color. This excess declines smoothly and is inconsistent with high transmission in the Lyα forest.

The spectrum shows no clear emission lines, and the most plausible explanation we could find is that this source could be a lensed quasar. In this scenario, the flux blueward of the break corresponds to a foreground source. If confirmed, this would make it only the second gravitationally lensed quasar known at $z > 5$ (see Fan et al. 2019; Taufik Andika et al. 2022). The closest visible source in the Pan-STARRS1 survey is 6″ away, too far for being the potential foreground lensed source. The extremely sharp break would imply a very small proximity zone, in line with the expectations for gravitationally lensed quasars (Davies et al. 2020). Moreover, the system is clearly detected in the DELS r_{DE} image (see Figure 3), with $r_{DE} = 23.11 \pm 0.09$ (and $g_{DE} > 25.1$ and $Z_{DE} = 20.31 \pm 0.02$). Detection in the r_{DE} is not expected for a source at $z = 6.4$, and this emission is likely coming from the potential foreground galaxy. We defer a more detailed analysis of the source to when we have further follow-up observations. Higher-resolution observations from space, Integral Field Unit observations, (sub) millimeter spectral line scans, and/or X-ray observations (e.g., Connor et al. 2021a) are required to confirm or provide supporting evidence for the lensing scenario.

As for redshift determination, the best-fitting template is weak-Lyα at $z = 6.35$, but all the other templates (except strong-Lyα, which would not apply here) yield $z = 6.41$, consistent with the observed Lyα break. Given the peculiarity of the source and the lack of clear features, we adopt $z = 6.41$ and use the template *yang2021* (the second best fit) to derive the rest-frame magnitudes, for which we do not attempt to correct for a possible magnification in this work.

3.5. VIK J1152+0055 (z = 6.3643)

This quasar was independently discovered by Matsuoka et al. (2016), and it has been widely studied since then. Decarli et al. (2018) and Izumi et al. (2018) studied the [C II] and cold dust properties with ALMA, while Onoue et al. (2019) measured the black hole mass from the Mg II emission line ($M_{BH} = 6.3 \times 10^8 \, M_{\odot}$). Our best-fitting template is *vandenberk2001*, yielding $z = 6.36$, in agreement with the more accurate [C II] redshift $z = 6.3643$ from Decarli et al. (2018).

3.5.1. PSO J265.9298+41.4139 (z = 6.0263)

P265+41 is a BAL quasar. Our best-fit template is the median-Lyα, yielding $z = 6.05$, and the second best fit is $z = 6.04$ with the *yang2021* template. However, if we fix the redshift derived from the [C II] observations ($z_{[C ii]} = 6.0263 \pm 0.0001$, Eilers et al. 2020), the best-fit template is *yang2021*, and we used this to derive the rest-frame magnitudes. P265+41 is the brightest quasar in [C II] and dust continuum emission studied by Eilers et al. (2020), indicating that the quasar resides in a starburst galaxy with a star formation rate (SFR) $\gtrsim 1470 \, M_{\odot} \, yr^{-1}$. We note that P265+41 has one of the reddest $y_{P1} - J$ colors. This is because the strong Si IV BAL falls exactly in the y_{P1} filter.

3.6. VIK J2211–3206 (z = 6.3394)

This is the brightest quasar of the sample ($M_{1450} = -28$), and it has already been part of a number of studies even before its discovery publication. J2211–3206 shows very strong BAL features that were studied by Bischetti et al. (2022). The [C II] and dust from the host galaxy was reported by Decarli et al. (2018) and HST imaging of the quasar and its environment was presented in Mazzucchelli et al. (2019). Our template redshift fails to find a good solution for a quasar with such strong BAL absorption. Bischetti et al. (2022) report a Mg II redshift $z = 6.330$, while Decarli et al. (2018) report a [C II] redshift $z = 6.3394$. We note that the Y and J bands are strongly contaminated by Si IV and C IV BAL absorption, and therefore it would be difficult to obtain the intrinsic rest-frame magnitudes from the observed spectrum. We use our strong-Lyα template at the [C II] redshift to estimate the rest-frame magnitudes.

3.7. VIK J2318–3029 (z = 6.1456)

Our best-fitting template is median-Lyα with $z = 6.14$, in good agreement with the [C II] redshift $z = 6.1456$ reported in Venemans et al. (2020).

3.8. Notes on Objects Not Satisfying the Selection Criteria

In this section, we discuss two Pan-STARRS1 quasars from an extended selection that would have not been selected using the criteria of Section 2.1.

3.8.1. PSO J030.1387–17.6238 (z = 6.09)

PSO J030.1387–17.6238 is from our extended selection as it has $S/N(z_{P1}) = 8.3$.

3.8.2. PSO J173.4601+48.2420 (z = 6.233)

This quasar would not have been selected due to its $S/N(y_{P1})$ <5. However, we selected this quasar following the more
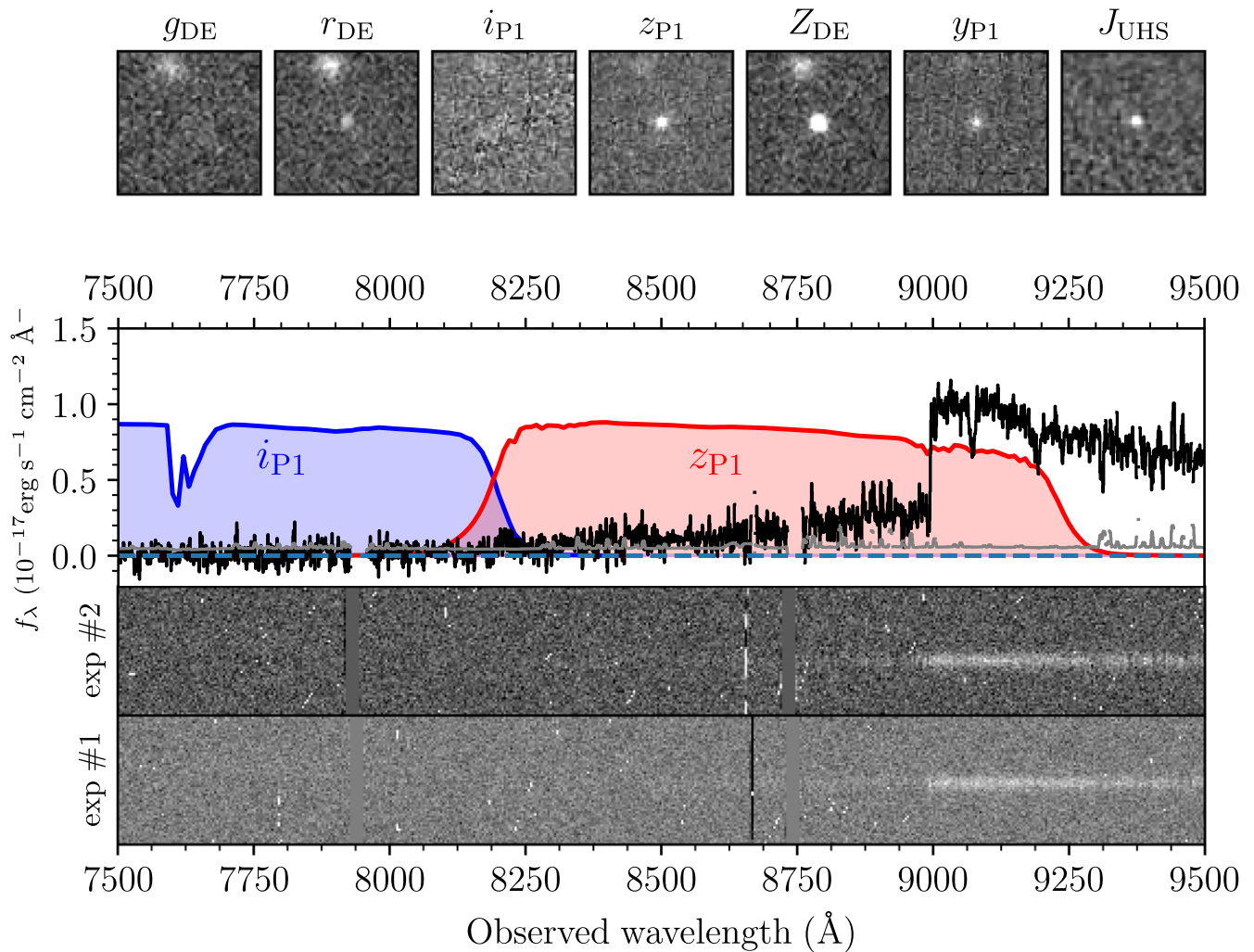
Figure 3. Gravitationally lensed quasar candidate P170+20 at $z = 6.41$. The extracted 1D spectrum (shown in black, and the 1σ error vector in gray) is the composite from the extraction of the two independent exposures shown at the bottom (sky-subtracted spectra, divided by the noise). In the 1D and 2D spectra, an excess of flux blueward of the sharp break is evident at $\sim$9000 Å. The top panel displays $15'' \times 15''$ postage stamps for images in the DELS, Pan-STARRS1, and UHS surveys. For reference, the i_{P1} and z_{P1} filter curves are overplotted on the 1D spectrum. The i_{P1} image is not reliable at the position of the quasar. The clear detection in the r_{DE} image is not expected for a source at $z = 6.4$ (the wavelength region is not covered by our spectrum).

relaxed selection presented in Bañados et al. (2015), which also required a radio counterpart in the Faint Images of the Radio Sky at Twenty-Centimeters survey (FIRST; Becker et al. 1995).

This quasar has a narrow Lyα line that is not represented in the templates used to estimate the redshift in Section 3.2. We use the redshift of a narrow absorption H I and N V system at $z = 6.233 \pm 0.003$, which might be associated with the host galaxy. The Lyα line is stronger than all templates except for strong-Lyα, but much narrower than the one in strong-Lyα. To estimate the rest-frame magnitudes, we fix the redshift to $z = 6.233$ and use the strong-Lyα template. This radio-loud quasar is further discussed in Section 4.

4. New Radio-loud Quasars

We cross-matched our 55 quasars with the FIRST survey (2014dec17 version), the LOFAR Two-meter Sky Survey DR2 (LoTSS-DR2; Shimwell et al. 2022), and the first data release of the Rapid ASKAP Continuum Survey (RACS; McConnell et al. 2020; Hale et al. 2021) catalogs. In the FIRST catalog, only P173+48 was detected. This detection was expected as a

FIRST counterpart was required for its selection (see Section 3.3). In the LoTSS-DR2 catalog, there are two matches: P173+48 and P207+37 (these two quasars were also recently reported by Gloudemans et al. 2022). In the RACS catalog, there are also two matches: P050−18 and P193−02.

We analyzed the FIRST, LoTSS, and RACS images following Bañados et al. (2015). We obtained $1' \times 1'$ ($2' \times 2'$ for RACS) images and checked whether there were S/N >3 detections within $2''$ ($4''$ for RACS) from the quasar positions. The FIRST footprint covers 24 of our quasars, and our procedure recovered two sources: P173+48, which was already in the FIRST catalog, and P193−02, which is detected at S/N = 3.4 with 509 ± 151 μJy (this last one was also part of the RACS catalog). The LoTSS-DR2 footprint covers 11 of our quasars, and we found three detections. In addition to the cataloged P173+48 and P207+37, we recover an S/N = 4.1 detection of P182+53 with 240 ± 60 μJy. The RACS footprint covers 40 of our quasars, and our procedure recovered the 2 cataloged quasars P050−18 and P193−02. We note that in the field of P193−02, there are another three radio sources within $2'$. The two closest ones are clearly associated with a group of foreground galaxies, while the source $\sim1.\!'2$ north of the quasar

does not have an obvious optical counterpart in Pan-STARRS1. There is an additional potential S/N = 3.9 $(0.94 \pm 0.24 \text{ mJy})$ source $4''1$ from P032–17, just outside our required matching radius, but still consistent with the typical positional uncertainties in the RACS survey. We do not consider P032–17 as radio loud, but we note that it is an interesting source for future follow-up to confirm whether this radio emission is real and coming from the quasar.

We followed the same procedure to analyze the quick-look images of the Very Large Array Sky Survey (VLASS; Lacy et al. 2020). VLASS provides two-epoch 3 GHz images of all the sky above decl. $-40°$, and it therefore covers all of our new quasars. We analyze the two VLASS epochs for each quasar and consider a detection robust only if the measurements are consistent within the two epochs. We recover two VLASS sources: P173+48 and P050–18. We report the radio properties of these five quasars in Table 4 and show their radio images in Figure 5.

In Table 4 we report the radio spectral index ($f_\nu \propto \nu^\alpha$) between the 144 MHz and 1.4 GHz ($\alpha_{1.4\,\text{GHz}}^{144\,\text{MHz}}$), 888 MHz and 1.4 GHz ($\alpha_{1.4\,\text{GHz}}^{0.9\,\text{GHz}}$), 888 MHz and 3 GHz ($\alpha_{3.0\,\text{GHz}}^{0.9\,\text{GHz}}$), and 1.4 GHz and 3 GHz ($\alpha_{3.0\,\text{GHz}}^{1.4\,\text{GHz}}$) when the data exist. We estimate the radio-loudness for our sources as $R_{2500} = f_{\nu,5\,\text{GHz}}/f_{\nu,2500\,\text{Å}}$. We estimate $f_{\nu,2500\,\text{Å}}$ from the rest-frame magnitudes, m_{2500}, listed in Table 2. To estimate the rest-frame flux density at 5 GHz, we extrapolate the observed radio emission using all the spectral slopes listed in Table 4, where we report the resulting range of R_{2500}. For sources only detected in LoTSS (P182+53 and P207 +37), we assume the median spectral index -0.29 as measured by Gloudemans et al. (2021). All five sources are classified as radio loud, i.e., with $R_{2500} > 10$ (see, e.g., Bañados et al. 2021); see Table 4.

4.1. Notes on Peculiar Radio-loud Quasars

4.1.1. PSO J173.4601+48.2420—Blazar Candidate

P173+48 at $z = 6.233$ is the brightest radio source in the sample. It is detected in all radio surveys that cover the quasar. Its two VLASS epochs differ by more than 2σ, which is suggestive of variability. The radio spectral $\alpha_{1.4\,\text{GHz}}^{144\,\text{MHz}} = -0.16$ and $\alpha_{3.0\,\text{GHz}}^{1.4\,\text{GHz}} = -0.41$ (VLASS epoch 1) are remarkably flat (the slightly steeper slope using VLASS epoch 2 $\alpha_{3.0\,\text{GHz}}^{1.4\,\text{GHz}} = -0.69$ can be due to variability). Both high variability and a flat radio spectral index ($-0.5 < \alpha < 0.5$) are indications of a blazar nature, i.e., a quasar with its relativistic jet pointing at a small angle from our line of sight (e.g., Caccianiga et al. 2019; Ighina et al. 2019). Monitoring the radio variability, simultaneous constraints on the radio spectral energy distribution, and X-ray observations can help to establish whether this radio-loud quasar is a blazar. If confirmed, this would be the most distant blazar known to date, with the current record at $z = 6.1$ (Belladitta et al. 2020).

We target the [C II] line (and underlying continuum) of the quasar with the NOEMA interferometer (program W21EC). The observations were carried out on 2021 December 13 with an on-source time of 7.5 hr. We reduced the data with GILDAS,[19] following the steps described in Khusanova et al. (2022). We used 3C84 and LKHA101 as bandpass and flux density calibrators, respectively.

---

[19] https://www.iram.fr/IRAMFR/GILDAS

Collapsing the entire datacube, except for the line containing channels ($\pm 1000 \text{ km s}^{-1}$ from the expected [C II] line location), we find a 3.5σ peak $\sim 1''$ offset from the optical position of the quasar (Figure 4). This signal might be noise given several positive and negative peaks of comparable significance. We extracted a spectrum centered on the 3.5σ peak described above and another one centered at the optical position of the quasar, finding no emission line in both cases. We created a line image averaging the channels from -150 to 150 km s^{-1} from the expected [C II] line. We find no significant detection on this image (middle panel of Figure 4).

We estimate a star formation rate (SFR) limit based on the continuum flux density, assuming a modified blackbody model with $T_{\text{dust}} = 47$ K and $\beta = 1.6$ (standard assumptions; see e.g., Decarli et al. 2018; Khusanova et al. 2022). Since a tentative detection is present in the continuum image, we use 5σ as a conservative upper limit for the SFR, yielding $< 69\, M_\odot\,\text{yr}^{-1}$ (using the conversion of Kennicutt 1998 with a Chabrier 2003 initial mass function). Assuming a [C II] line width of 300 km s^{-1}, the 3σ upper limit on the SFR is 27 $M_\odot\,\text{yr}^{-1}$ (using the conversion of De Looze et al. 2014). Only one other $z \gtrsim 6$ radio-loud quasar has remained undetected in both [C II] and the underlying continuum with observations of similar depth (Khusanova et al. 2022).

4.1.2. PSO J193.3992–02.7820—Radio Transient?

P193–02 has a strong RACS detection, but the relatively weak 3.4σ FIRST detection implies an ultrasteep radio spectrum with $\alpha \approx -4.6$. Taking the radio spectral index at face value would make it the radio-loudest quasar in the sample with $R_{2500} \approx 1300$. We note, however, that there is a significant difference between the integrated and peak flux densities (4.05 ± 0.07 mJy versus 2.86 ± 0.02 mJy). This discrepancy could mean that the source is extended or that multiple sources contribute to the integrated flux density. Even if we consider the peak flux density, this results in an ultrasteep spectrum with $\alpha \approx -3.8$ and high radio-loudness $R_{2500} \approx 800$. The steep radio spectrum is in agreement with the nondetection in VLASS. Ultrasteep radio sources are expected to be lobe dominated, and this signature is often used to find high-redshift radio galaxies (e.g., Saxena et al. 2018a). Interestingly, the implied steep radio slope for this source makes it an extreme outlier: there are virtually no quasars or radio galaxies known with such a steep radio spectrum (see Saxena et al. 2018b; Sabater et al. 2019; Zajaček et al. 2019; Bañados et al. 2021). If this steep slope continues to lower frequencies without a turnover, we would expect unprecedented radio emission at a Jansky level at about 200 MHz. However, the quasar is undetected in the TIFR GMRT Sky Survey (TGSS; Intema et al. 2017) at 147.5 MHz. We analyze the TGSS image and obtain a 3σ upper limit of 7.1 mJy (we note that none of the new radio-loud quasars presented in this paper are detected in TGSS). This nondetection implies a substantial turnover between 147.5 and 888 MHz.

Another possibility is that the strong RACS detection of P193–02 was a radio transient (e.g., Mooley et al. 2016). A flux density of 4.1 mJy translates into a specific luminosity of $L_\nu = 2.2 \times 10^{33} \text{ erg s}^{-1} \text{ Hz}^{-1}$ at the redshift of the quasar, which is brighter than the most radio luminous supernovae or gamma-ray bursts ever observed, but consistent with an AGN flare (Pietka et al. 2015; Nyland et al. 2020). We note that the strong RACS emission detected on 2020 May 1 happened

Table 4
Properties of the Quasars Detected in Public Radio Surveys, Sorted by R.A.

Quasar	z	LoTTS$_{144\ MHz}$ (μJy)	LoTTS ref	RACS$_{888\ MHz}$ (μJy)	RACS ref	FIRST$_{1.4\ GHz}$ (μJy)	FIRST ref	VLASS$_{3\ GHz}$ Ep 1 (μJy)	VLASS$_{3\ GHz}$ Ep 2 (μJy)	VLASS ref [a]	$\alpha^{144\ MHz}_{1.4\ GHz}$	$\alpha^{0.9\ GHz}_{1.4\ GHz}$	$\alpha^{0.9\ GHz}_{3.0\ GHz}$	$\alpha^{1.4\ GHz}_{3.0\ GHz}$	R_{2500}
P050–18	6.09	...	...	1905 ± 350	DR1	...	...	749 ± 183	738 ± 153	1.2/2.2	...	...	−0.77 ± 0.25	...	156 ± 31
P173+48	6.233	4673 ± 323	DR2	...	...	3226 ± 135	v2014dec17	2360 ± 140	1910 ± 150	1.2/2.2	−0.16 ± 0.04	...	...	−0.41 ± 0.10/ − 0.69 ± 0.12	734 − 1067
P182+53	5.99	240 ± 58	forced	...	...	<438	forced	<349	<419	1.1/2.1	<0.26	...	...	...	18 ± 4
P193–02[b]	5.8	...	...	4048 ± 660	DR1	509 ± 151	forced	<496	<438	1.2/2.2	...	−4.55 ± 0.74	< − 1.83	...	108 − 1315
P207+37	5.69	485 ± 151	DR2	<615	forced	<440	forced	<370	<409	1.1/2.1	< − 0.04	...	...	...	27 ± 9

Notes. A reference "forced" means that there was no entry in the catalog and we measured the flux from the images. For VLASS, we always measure the peak flux densities directly from the images.
[a] The peak flux densities for the VLASS1.1 epoch are known to be systematically low by ≈15% and by ≈8% for the subsequent epochs (1.2/2.1/2.2); see https://science.nrao.edu/vlass/data-access/vlass-epoch-1-quick-look-users-guide. We have taken these factors into account in the reported values.
[b] The radio-loudness of P193–02 is very uncertain because its strong RACS detection could have been an AGN flare; see the discussion in Section 4.
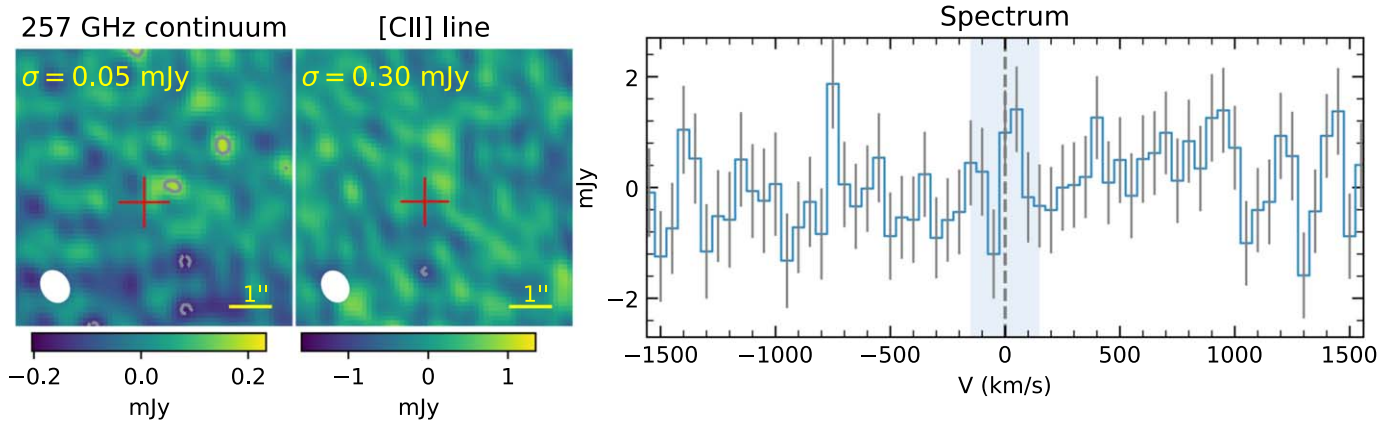
Figure 4. NOEMA observations of the blazar candidate P173+48. Left: The 257 GHz continuum image (the entire datacube), excluding the channels around the expected [C II] emission line (shaded area in the right panel). Middle: The integrated image obtained by averaging the channels around the expected [C II] emission line (shaded area in the right panel). In the left and middle panels, the contour levels are $(-3, 3) \times \sigma$, and the red cross shows the optical position of the quasar. Right: Spectrum extracted from the 3.5σ peak $\sim 1''$ from the optical position of the quasar (see left panel). The dashed vertical line shows the expected location of the [C II] line at $z = 6.233$.
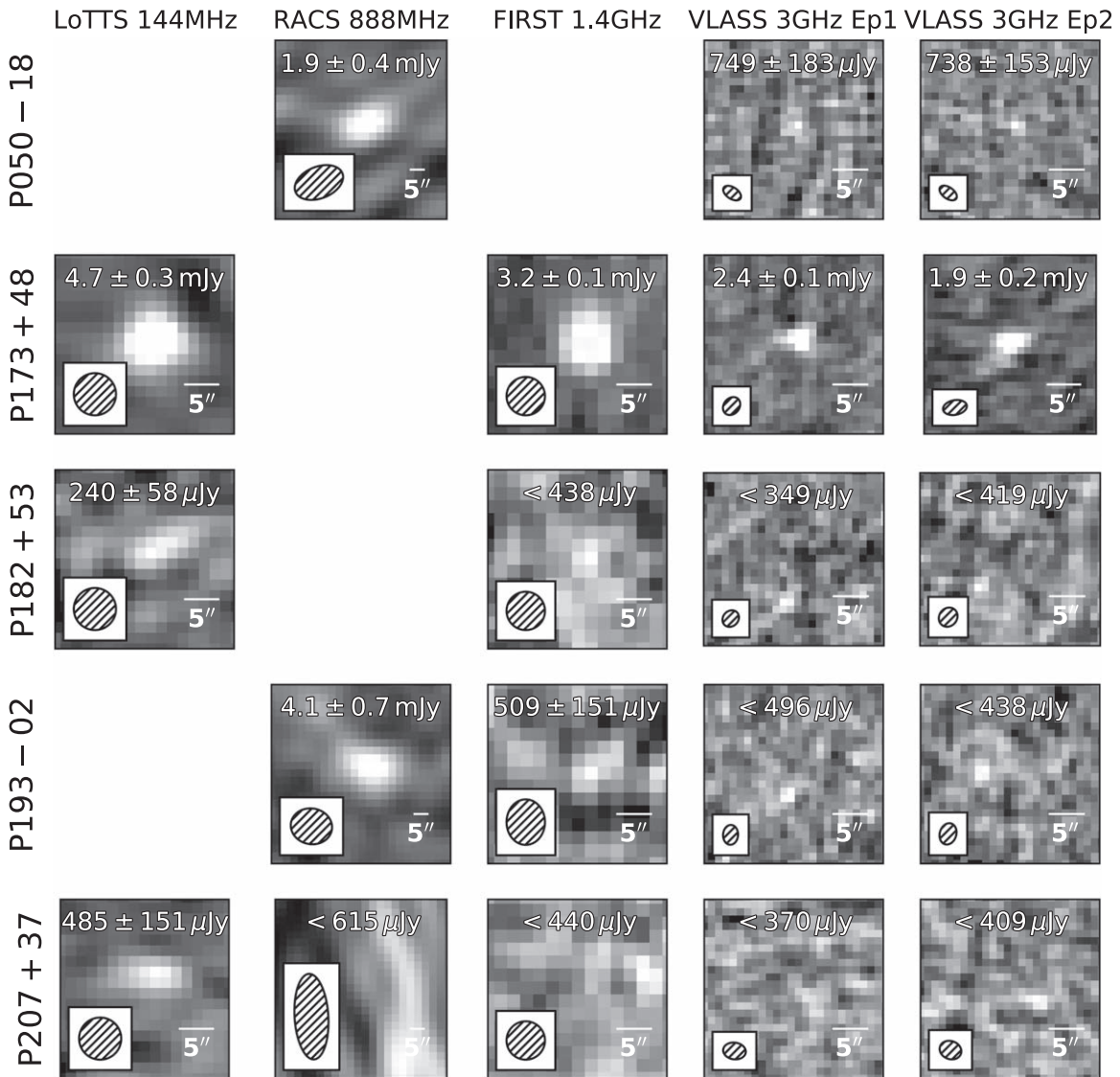
Figure 5. $25'' \times 25''$ ($60'' \times 60''$ for RACS) radio images for the quasars detected in at least one of the following radio surveys: LoTSS-DR2 (left column), RACS (second column), FIRST (third column), or both VLASS epochs (fourth and fifth columns). The measured flux density (or limits) are shown at the top of each postage stamp, and the beam sizes are indicated in the bottom left corner of each image. See Section 4.

between the nondetections in the two VLASS epochs (2019 April 21 and 2021 December 12). The whole period is just about 5 months in the quasar rest frame. Assuming a more realistic steep radio spectral index $\alpha = -1$, given the RACS detection we would expect a 1.2 mJy source in VLASS. The fact that we do not detect it implies that the source should have increased its luminosity by at least a factor of 3 in a rest frame of about 2 months and faded by the same factor in a rest frame of about 3 months. This rapid variability suggests blazar-like activity (Pietka et al. 2015). Assuming that the FIRST flux density is representative of its steady state and assuming $\alpha = -0.63$ (median value used in Bañados et al. 2021 for objects without a measured radio slope), P193–02 would still be classified as radio loud with $R_{2500} \approx 100$.

Another possibility is that at least part of the RACS emission is associated with a lobe of a radio galaxy at $z = 0.4$, whose core emission is $25''$ to the northeast of P193–02. This scenario would explain the observed steep radio slope. Nevertheless, the radio properties of P193–02 are puzzling, and an additional epoch at 888 MHz and/or higher-resolution/deeper observations are required to understand this source better.

5. Summary

In this paper, we present the discovery of 55 quasars at $5.6 < z < 6.5$, continuing the work from Bañados et al. (2016) and Venemans et al. (2015), to select high-redshift quasars with the Pan-STARRS1 and VIKING surveys, respectively. Our selection function for $z \sim 6$ Pan-STARRS1 quasars is discussed and is used to derive the $z \sim 6$ quasar luminosity function in the companion paper by Schindler et al. (2023).

The quasars presented here show a range of properties, including objects with weak emission line quasars and BAL quasars, which seem more common at $z \sim 6$ than at lower redshifts (see, e.g., Bañados et al. 2016; Bischetti et al. 2022). Nine percent of the quasars presented here are radio loud, including one blazar candidate. This percentage is in line with the expectations (e.g., Bañados et al. 2015; Liu et al. 2021). We also present a $z = 6.41$ quasar that could be the second gravitationally lensed quasar known at $z > 5$. Multiwavelength follow-up observations of the quasars presented in this sample are required to understand their nature and physical properties better.

Two of the VIKING quasars could have been selected by the Pan-STARRS1 selection if we had relaxed our S/N requirements. The additional discoveries just below our nominal S/N cuts demonstrate that there are still more high-redshift quasars to be found in the Pan-STARRS1 survey (Section 3.8), likely at the expense of significantly higher contamination. Given the existence of large sky radio surveys, including recent ones such as LoTSS, RACS, and VLASS (see Figure 5), relaxing our S/N and/or color requirements described in Section 2, but requiring a radio detection, could be a promising way to expose some of the quasar populations we are currently missing. Eventually, the advent of large multiobject spectroscopic surveys such as 4MOST (de Jong et al. 2019) and DESI (Chaussidon et al. 2022) will be fundamental to maximize the discovery of quasars that are located in a color space that is dominated by other astronomical sources and/or that are at the limits of current selections.

ORCID iDs

Eduardo Bañados ⓘ https://orcid.org/0000-0002-2931-7824
Jan-Torge Schindler ⓘ https://orcid.org/0000-0002-4544-8242
Bram P. Venemans ⓘ https://orcid.org/0000-0001-9024-8322
Thomas Connor ⓘ https://orcid.org/0000-0002-7898-7664
Roberto Decarli ⓘ https://orcid.org/0000-0002-2662-8803
Emanuele Paolo Farina ⓘ https://orcid.org/0000-0002-6822-2254
Chiara Mazzucchelli ⓘ https://orcid.org/0000-0002-5941-5214
Romain A. Meyer ⓘ https://orcid.org/0000-0001-5492-4522
Daniel Stern ⓘ https://orcid.org/0000-0003-2686-9241
Fabian Walter ⓘ https://orcid.org/0000-0003-4793-7880
Xiaohui Fan ⓘ https://orcid.org/0000-0003-3310-0131
Joseph F. Hennawi ⓘ https://orcid.org/0000-0002-7054-4332
Yana Khusanova ⓘ https://orcid.org/0000-0002-7220-397X
Nidia Morrell ⓘ https://orcid.org/0000-0003-2535-3091
Riccardo Nanni ⓘ https://orcid.org/0000-0002-2579-4789
Antonio Pensabene ⓘ https://orcid.org/0000-0001-9815-4953
Hans-Walter Rix ⓘ https://orcid.org/0000-0003-4996-9069
Joseph Simon ⓘ https://orcid.org/0000-0003-1407-6607
Gijs A. Verdoes Kleijn ⓘ https://orcid.org/0000-0001-5803-2580
Zhang-Liang Xie (谢彰亮) ⓘ https://orcid.org/0000-0002-0125-6679
Da-Ming Yang (羊达明) ⓘ https://orcid.org/0000-0002-6769-0910
Andrew Connor ⓘ https://orcid.org/0000-0002-4886-8664

References

Abbott, T. M. C., Abdalla, F. B., Allam, S., et al. 2018, ApJS, 239, 18
Abbott, T. M. C., Adamów, M., Aguena, M., et al. 2021, ApJS, 255, 20
Appenzeller, I., & Rupprecht, G. 1992, Msngr, 67, 18
Astropy Collaboration, Price-Whelan, A. M., Sipőcz, B. M., et al. 2018, AJ, 156, 123
Astropy Collaboration, Robitaille, T. P., Tollerud, E. J., et al. 2013, A&A, 558, A33
Bañados, E., Venemans, B. P., Morganson, E., et al. 2014, AJ, 148, 14
Bañados, E., Venemans, B. P., Morganson, E., et al. 2015, ApJ, 804, 118
Bañados, E., Venemans, B. P., Decarli, R., et al. 2016, ApJS, 227, 11
Bañados, E., Venemans, B. P., Mazzucchelli, C., et al. 2018, Natur, 553, 473
Bañados, E., Rauch, M., Decarli, R., et al. 2019, ApJ, 885, 59
Bañados, E., Mazzucchelli, C., Momjian, E., et al. 2021, ApJ, 909, 80
Becker, R. H., White, R. L., & Helfand, D. J. 1995, ApJ, 450, 559
Belladitta, S., Moretti, A., Caccianiga, A., et al. 2020, A&A, 635, L7
Bischetti, M., Feruglio, C., D'Odorico, V., et al. 2022, Natur, 605, 244
Bosman, S. E. I., Davies, F. B., Becker, G. D., et al. 2022, MNRAS, 514, 55
Caccianiga, A., Moretti, A., Belladitta, S., et al. 2019, MNRAS, 484, 204
Chabrier, G. 2003, PASP, 115, 763
Chambers, K. C., Magnier, E. A., Metcalfe, N., et al. 2016, arXiv:1612.05560
Chaussidon, E., Yèche, C., Palanque-Delabrouille, N., et al. 2022, arXiv:2208.08511
Chehade, B., Carnall, A. C., Shanks, T., et al. 2018, MNRAS, 478, 1649
Chen, S.-F. S., Simcoe, R. A., Torrey, P., et al. 2017, ApJ, 850, 188
Connor, T., Stern, D., Bañados, E., & Mazzucchelli, C. 2021a, ApJL, 922, L24
Connor, T., Bañados, E., Stern, D., et al. 2021b, ApJ, 911, 120
Connor, T., Bañados, E., Stern, D., et al. 2019, ApJ, 887, 171
Cooper, T. J., Simcoe, R. A., Cooksey, K. L., et al. 2019, ApJ, 882, 771
Davies, F. B., Wang, F., Eilers, A.-C., & Hennawi, J. F. 2020, ApJL, 904, L32
de Jong, R. S., Agertz, O., Berbel, A. A., et al. 2019, Msngr, 175, 3
De Looze, I., Cormier, D., Lebouteiller, V., et al. 2014, A&A, 568, A62
Decarli, R., Walter, F., Venemans, B. P., et al. 2017, Natur, 545, 457
Decarli, R., Walter, F., Venemans, B. P., et al. 2018, ApJ, 854, 97
Decarli, R., Dotti, M., Bañados, E., et al. 2019, ApJ, 880, 157
Decarli, R., Pensabene, A., Venemans, B., et al. 2022, A&A, 662, A60
Dey, A., Schlegel, D. J., Lang, D., et al. 2019, AJ, 157, 168
Drake, A. B., Neeleman, M., Venemans, B. P., et al. 2022, ApJ, 929, 86

Dye, S., Lawrence, A., Read, M. A., et al. 2018, MNRAS, 473, 5113
Edge, A., Sutherland, W., Kuijken, K., et al. 2013, Msngr, 154, 32
Eilers, A.-C., Hennawi, J. F., Decarli, R., et al. 2020, ApJ, 900, 37
Fan, X., Wang, F., Yang, J., et al. 2019, ApJL, 870, L11
Farina, E. P., Venemans, B. P., Decarli, R., et al. 2017, ApJ, 848, 78
Farina, E. P., Arrigoni-Battaia, F., Costa, T., et al. 2019, ApJ, 887, 196
Farina, E. P., Schindler, J.-T., Walter, F., et al. 2022, ApJ, 941, 106
Freudling, W., Romaniello, M., Bramich, D. M., et al. 2013, A&A, 559, A96
Gaia Collaboration, Prusti, T., de Bruijne, J. H. J., et al. 2016, A&A, 595, A1
Gaia Collaboration, Brown, A. G. A., Vallenari, A., et al. 2021, A&A, 649, A1
Gaikwad, P., Rauch, M., Haehnelt, M. G., et al. 2020, MNRAS, 494, 5091
Gloudemans, A. J., Duncan, K. J., Röttgering, H. J. A., et al. 2021, A&A, 656, A137
Gloudemans, A. J., Duncan, K. J., Saxena, A., et al. 2022, A&A, 668, A27
Greiner, J., Bolmer, J., Yates, R. M., et al. 2021, A&A, 654, A79
Greiner, J., Bornemann, W., Clemens, C., et al. 2008, PASP, 120, 405
Hale, C. L., McConnell, D., Thomson, A. J. M., et al. 2021, PASA, 38, e058
Harris, C. R., Millman, K. J., van der Walt, S. J., et al. 2020, Natur, 585, 357
Hook, I. M., Jørgensen, I., Allington-Smith, J. R., et al. 2004, PASP, 116, 425
Hunter, J. D. 2007, CSE, 9, 90
Ighina, L., Caccianiga, A., Moretti, A., et al. 2019, MNRAS, 489, 2732
Intema, H. T., Jagannathan, P., Mooley, K. P., & Frail, D. A. 2017, A&A, 598, A78
Izumi, T., Onoue, M., Shirakata, H., et al. 2018, PASJ, 70, 36
Kennicutt, R. C., Jr. 1998, ApJ, 498, 541
Khusanova, Y., Bañados, E., Mazzucchelli, C., et al. 2022, A&A, 664, A39
Kuijken, K., Heymans, C., Dvornik, A., et al. 2019, A&A, 625, A2
Lacy, M., Baum, S. A., Chandler, C. J., et al. 2020, PASP, 132, 035001
Lai, S., Bian, F., Onken, C. A., et al. 2022, MNRAS, 513, 1801
Lawrence, A., Warren, S. J., Almaini, O., et al. 2007, MNRAS, 379, 1599
Li, Q., Wang, R., Fan, X., et al. 2020, ApJ, 900, 12
Liu, Y., Wang, R., Momjian, E., et al. 2021, ApJ, 908, 124
Lubow, S. H., White, R. L., & Shiao, B. 2021, AJ, 161, 6
Magnier, E. A., Sweeney, W. E., Chambers, K. C., et al. 2020, ApJS, 251, 5
Matsuoka, Y., Onoue, M., Kashikawa, N., et al. 2016, ApJ, 828, 26
Matsuoka, Y., Iwasawa, K., Onoue, M., et al. 2018, ApJS, 237, 5
Matsuoka, Y., Iwasawa, K., Onoue, M., et al. 2022, ApJS, 259, 18
Mazzucchelli, C., Bañados, E., Decarli, R., et al. 2017a, ApJ, 834, 83
Mazzucchelli, C., Bañados, E., Venemans, B. P., et al. 2017b, ApJ, 849, 91
Mazzucchelli, C., Decarli, R., Farina, E. P., et al. 2019, ApJ, 881, 163
McConnell, D., Hale, C. L., Lenc, E., et al. 2020, PASA, 37, e048
McMahon, R. G., Banerji, M., Gonzalez, E., et al. 2013, Msngr, 154, 35
Meyer, R. A., Bosman, S. E. I., & Ellis, R. S. 2019, MNRAS, 487, 3305
Meyer, R. A., Kakiichi, K., Bosman, S. E. I., et al. 2020, MNRAS, 494, 1560
Meyer, R. A., Decarli, R., Walter, F., et al. 2022, ApJ, 927, 141
Momjian, E., Bañados, E., Carilli, C. L., Walter, F., & Mazzucchelli, C. 2021, AJ, 161, 207
Momjian, E., Carilli, C. L., Bañados, E., Walter, F., & Venemans, B. P. 2018, ApJ, 861, 86
Mooley, K. P., Hallinan, G., Bourke, S., et al. 2016, ApJ, 818, 105
Moorwood, A., Cuby, J.-G., & Lidman, C. 1998, Msngr, 91, 9
Mortlock, D. J., Patel, M., Warren, S. J., et al. 2012, MNRAS, 419, 390

Novak, M., Venemans, B. P., Walter, F., et al. 2020, ApJ, 904, 131
Nyland, K., Dong, D. Z., Patil, P., et al. 2020, ApJ, 905, 74
Oke, J. B., & Gunn, J. E. 1982, PASP, 94, 586
Oke, J. B., Cohen, J. G., Carr, M., et al. 1995, PASP, 107, 375
Onoue, M., Kashikawa, N., Matsuoka, Y., et al. 2019, ApJ, 880, 77
Pensabene, A., Decarli, R., Bañados, E., et al. 2021, A&A, 652, A66
Pensabene, A., van der Werf, P., Decarli, R., et al. 2022, A&A, 667, A9
Pietka, M., Fender, R. P., & Keane, E. F. 2015, MNRAS, 446, 3687
Pogge, R. W., Atwood, B., Brewer, D. F., et al. 2010, Proc. SPIE, 7735, 77350A
Prochaska, J. X., Hennawi, J. F., Westfall, K. B., et al. 2020a, JOSS, 5, 2308
Prochaska, J. X., Hennawi, J., Cooke, R., et al. 2020b, pypeit/PypeIt: Release, v1.0.0 Zenodo, doi:10.5281/zenodo.3743493
Reed, S. L., McMahon, R. G., Martini, P., et al. 2017, MNRAS, 468, 4702
Rojas-Ruiz, S., Bañados, E., Neeleman, M., et al. 2021, ApJ, 920, 150
Ross, N. P., & Cross, N. J. G. 2020, MNRAS, 494, 789
Sabater, J., Best, P. N., Hardcastle, M. J., et al. 2019, A&A, 622, A17
Saxena, A., Marinello, M., Overzier, R. A., et al. 2018a, MNRAS, 480, 2733
Saxena, A., Jagannathan, P., Röttgering, H. J. A., et al. 2018b, MNRAS, 475, 5041
Schindler, J.-T., Farina, E. P., Bañados, E., et al. 2020, ApJ, 905, 51
Schindler, J.-T., Bañados, E., Connor, T., et al. 2023, ApJ, 943, 67
Schlafly, E. F., & Finkbeiner, D. P. 2011, ApJ, 737, 103
Schlegel, D. J., Finkbeiner, D. P., & Davis, M. 1998, ApJ, 500, 525
Schmidt, G. D., Weymann, R. J., & Foltz, C. B. 1989, PASP, 101, 713
Selsing, J., Fynbo, J. P. U., Christensen, L., & Krogager, J.-K. 2016, A&A, 585, A87
Shen, Y., Wu, J., Jiang, L., et al. 2019, ApJ, 873, 35
Shimwell, T. W., Hardcastle, M. J., Tasse, C., et al. 2022, A&A, 659, A1
Snodgrass, C., Saviane, I., Monaco, L., & Sinclaire, P. 2008, Msngr, 132, 18
Stevenson, K. B., Bean, J. L., Seifahrt, A., et al. 2016, ApJ, 817, 141
Taufik Andika, I., Jahnke, K., van der Wel, A., et al. 2022, arXiv:2211.14543
Taylor, M. B. 2005, in ASP Conf. Ser. 347, Astronomical Data Analysis Software and Systems XIV, ed. P. Shopbell, M. Britton, & R. Ebert (San Francisco, CA: ASP), 29
Tody, D. 1986, Proc. SPIE, 627, 733
van Haarlem, M. P., Wise, M. W., Gunst, A. W., et al. 2013, A&A, 556, A2
Vanden Berk, D. E., Richards, G. T., Bauer, A., et al. 2001, AJ, 122, 549
Venemans, B. P., Findlay, J. R., Sutherland, W. J., et al. 2013, ApJ, 779, 24
Venemans, B. P., Verdoes Kleijn, G. A., Mwebaze, J., et al. 2015, MNRAS, 453, 2259
Venemans, B. P., Decarli, R., Walter, F., et al. 2018, ApJ, 866, 159
Venemans, B. P., Walter, F., Neeleman, M., et al. 2020, ApJ, 904, 130
Virtanen, P., Gommers, R., Oliphant, T. E., et al. 2020, NatMe, 17, 261
Vito, F., Brandt, W. N., Bauer, F. E., et al. 2019, A&A, 630, A118
Vito, F., Brandt, W. N., Ricci, F., et al. 2021, A&A, 649, A133
Wang, F., Yang, J., Fan, X., et al. 2019, ApJ, 884, 30
Wang, R., Wagg, J., Carilli, C. L., et al. 2011, ApJL, 739, L34
Wang, R., Wagg, J., Carilli, C. L., et al. 2013, ApJ, 773, 44
Wang, S., Jiang, L., Shen, Y., et al. 2022, ApJ, 925, 121
Yang, J., Wang, F., Fan, X., et al. 2021, ApJ, 923, 262
Zajaček, M., Busch, G., Valencia, S. M., et al. 2019, A&A, 630, A83